

THE ATACAMA COSMOLOGY TELESCOPE: LIKELIHOOD FOR SMALL-SCALE CMB DATA

J. DUNKLEY¹, E. CALABRESE¹, J. SIEVERS², G. E. ADDISON^{3,1}, N. BATTAGLIA⁴, E. S. BATTISTELLI⁵, J. R. BOND⁶, S. DAS^{7,8}, M. J. DEVLIN⁹, R. DÜNNER¹⁰, J. W. FOWLER¹¹, M. GRALLA¹², A. HAJIAN⁶, M. HALPERN³, M. HASSELFIELD^{13,3}, A. D. HINCKS⁶, R. HLOZEK^{13,2}, J. P. HUGHES¹⁴, K. D. IRWIN¹¹, A. KOSOWSKY¹⁵, T. LOUIS¹, T. A. MARRIAGE^{12,13,2}, D. MARSDEN^{9,16}, F. MENANTEAU¹⁴, K. MOODLEY¹⁷, M. NIEMACK^{18,11}, M. R. NOLTA⁶, L. A. PAGE², B. PARTRIDGE¹⁹, N. SEHGAL²⁰, D. N. SPERGEL¹³, S. T. STAGGS², E. R. SWITZER⁶, H. TRAC⁴, E. WOLLACK²¹

¹ Sub-department of Astrophysics, University of Oxford, Keble Road, Oxford OX1 3RH, UK

² Joseph Henry Laboratories of Physics, Jadwin Hall, Princeton University, Princeton, NJ, USA 08544

³ Department of Physics and Astronomy, University of British Columbia, Vancouver, BC, Canada V6T 1Z4

⁴ McWilliams Center for Cosmology, Wean Hall, Carnegie Mellon University, 5000 Forbes Ave., Pittsburgh PA 15213, USA

⁵ Department of Physics, University of Rome ‘La Sapienza’, Piazzale Aldo Moro 5, I-00185 Rome, Italy

⁶ Canadian Institute for Theoretical Astrophysics, University of Toronto, Toronto, ON, Canada M5S 3H8

⁷ High Energy Physics Division, Argonne National Laboratory, 9700 S Cass Avenue, Lemont IL 60439, USA

⁸ Berkeley Center for Cosmological Physics, LBL and Department of Physics, University of California, Berkeley, CA, USA 94720

⁹ Department of Physics and Astronomy, University of Pennsylvania, 209 South 33rd Street, Philadelphia, PA, USA 19104

¹⁰ Departamento de Astronomía y Astrofísica, Pontificia Universidad Católica de Chile, Casilla 306, Santiago 22, Chile

¹¹ NIST Quantum Devices Group, 325 Broadway Mailcode 817.03, Boulder, CO, USA 80305

¹² Dept. of Physics and Astronomy, The Johns Hopkins University, 3400 N. Charles St., Baltimore, MD 21218-2686, USA

¹³ Department of Astrophysical Sciences, Peyton Hall, Princeton University, Princeton, NJ USA 08544

¹⁴ Department of Physics and Astronomy, Rutgers, The State University of New Jersey, Piscataway, NJ USA 08854-8019

¹⁵ Department of Physics and Astronomy, University of Pittsburgh, Pittsburgh, PA, USA 15260

¹⁶ Department of Physics, University of California Santa Barbara, CA 93106, USA

¹⁷ Astrophysics and Cosmology Research Unit, School of Mathematical Sciences, University of KwaZulu-Natal, Durban, 4041, South Africa

¹⁸ Department of Physics, Cornell University, Ithaca, NY, USA 14853

¹⁹ Department of Physics and Astronomy, Haverford College, Haverford, PA, USA 19041

²⁰ Stony Brook University, Physics and Astronomy Department, Stony Brook, NY, USA 11794 and

²¹ NASA/Goddard Space Flight Center, Greenbelt, MD, USA 20771

Draft version October 29, 2018

ABSTRACT

The Atacama Cosmology Telescope has measured the angular power spectra of microwave fluctuations to arcminute scales at frequencies of 148 and 218 GHz, from three seasons of data. At small scales the fluctuations in the primordial Cosmic Microwave Background (CMB) become increasingly obscured by extragalactic foregrounds and secondary CMB signals. We present results from a nine-parameter model describing these secondary effects, including the thermal and kinematic Sunyaev-Zel’dovich (tSZ and kSZ) power; the clustered and Poisson-like power from Cosmic Infrared Background (CIB) sources, and their frequency scaling; the tSZ-CIB correlation coefficient; the extragalactic radio source power; and thermal dust emission from Galactic cirrus in two different regions of the sky. In order to extract cosmological parameters, we describe a likelihood function for the ACT data, fitting this model to the multi-frequency spectra in the multipole range $500 < \ell < 10000$. We extend the likelihood to include spectra from the South Pole Telescope at frequencies of 95, 150, and 220 GHz. Accounting for different radio source levels and Galactic cirrus emission, the same model provides an excellent fit to both datasets simultaneously, with $\chi^2/\text{dof} = 675/697$ for ACT, and 96/107 for SPT. We then use the multi-frequency likelihood to estimate the CMB power spectrum from ACT in bandpowers, marginalizing over the secondary parameters. This provides a simplified ‘CMB-only’ likelihood in the range $500 < \ell < 3500$ for use in cosmological parameter estimation.

Subject headings: cosmology: cosmic microwave background, cosmology: observations

1. INTRODUCTION

Measurements of the Cosmic Microwave Background (CMB) have played a central role in constraining cosmological models. Anisotropies measured over the whole sky by WMAP have provided evidence for a flat universe described by just six cosmological parameters. The measurement of the Sachs-Wolfe plateau in the power spectrum, and three acoustic peaks, have led to constraints on Λ CDM parameters to percent-level accuracy (Komatsu et al. 2011; Larson et al. 2011). The Silk damping tail of the power spectrum provides a wealth of additional information about the physics of the early universe, encoded in its shape, and in the positions and heights of the higher-order acoustic peaks (Silk 1968).

Extracting information from these angular scales is complicated by the presence of additional power from extragalactic point sources, emission from the Galaxy, and secondary anisotropies due to the thermal and kinematic Sunyaev-Zel’dovich effects (Sunyaev & Zel’dovich 1970).

The Atacama Cosmology Telescope (ACT) mapped the mm-wave sky with arcminute resolution from 2007 to 2010 in two distinct areas. About 600 square degrees were used to compute the angular power spectrum. Power spectra and cosmological results using the 1-year data, from the 2008 observing season, were presented in Fowler et al. (2010); Das et al. (2011); and Dunkley et al. (2011). During roughly the same period, the South Pole Telescope also mapped the

microwave sky, and presented cosmological results in Lueker et al. (2010); Shirokoff et al. (2011); Keisler et al. (2011); Reichardt et al. (2012); and Story et al. (2012).

In this paper we describe a method to fit multi-frequency power spectra from the ACT data simultaneously for CMB, foreground, and SZ parameters, following a similar approach to analyses in Dunkley et al. (2011) and Reichardt et al. (2012). We describe the likelihood constructed for the 3-year ACT dataset, using data from the 2008-2010 observing seasons, and show how it can be used in combination with data from SPT in a self-consistent way. Using this likelihood from ACT, we then construct a simpler CMB-only likelihood, estimating CMB bandpowers marginalized over the SZ and foreground parameters.

This is one of a set of papers on the 3-year ACT data; Das et al. (2013) present the angular power spectra, and Sievers et al. (2013) use the likelihoods presented here to estimate cosmological parameters. We begin in §2 by describing the model for the mm-wave emission. In §3 the full likelihood of the ACT data is described, including the combination with data from SPT and WMAP 7-year data. In §4 we show the small-scale model fit to the multi-frequency data. In §5 we describe the compressed CMB-only likelihood, concluding in §6.

2. MODEL FOR THE MM-WAVE SKY

Sky maps of mm-wave fluctuations at arcminute resolution include components emitting at low redshift, in addition to the primordial CMB signal and secondary CMB effects (e.g., Sievers et al. 2009; Fowler et al. 2010; Dunkley et al. 2011; Keisler et al. 2011). The power spectra from the complete ACT dataset, reported in Das et al. (2013), are shown in Figure 1, focusing on angular scales of interest for the primordial CMB signal. At scales smaller than a few arcminutes ($\ell \simeq 1500$) the secondary signal, which we define as the sum of foregrounds and SZ effects, becomes significant compared to the CMB. We want to extract the primary CMB signal, but, since there are more foreground components than frequency channels, information about both the frequency and scale dependence of the foregrounds is required to separate the signals. In this section we describe a model to fit the power spectrum of these fluctuations over the frequency range $90 \lesssim \nu \lesssim 250$ GHz probed by ACT, SPT, and other CMB experiments including the *Planck* satellite (Planck Collaboration I et al. 2011). We follow a similar approach to Sievers et al. (2009); Dunkley et al. (2011); Reichardt et al. (2012).

For frequency ν and direction $\hat{\mathbf{n}}$ we model the signal in the maps as

$$\Delta T(\nu, \hat{\mathbf{n}}) = \Delta T^{\text{CMB}}(\hat{\mathbf{n}}) + \Delta T^{\text{sec}}(\nu, \hat{\mathbf{n}}), \quad (1)$$

where $\Delta T^{\text{CMB}}(\hat{\mathbf{n}})$ are the lensed CMB fluctuations, which are independent of frequency in thermodynamic units. The secondary signal, $\Delta T^{\text{sec}}(\nu, \hat{\mathbf{n}})$, is dominated by the sum of tSZ and kSZ components, emission from dusty infrared galaxies and radio galaxies, and dust emission from Galactic cirrus, all of which are functions of frequency.

The cross-correlation power spectra between frequency ν_i and ν_j are calculated as

$$C_\ell^{\text{ij}} = \left\langle \tilde{T}_\ell^*(\nu_i) \tilde{T}_\ell(\nu_j) \right\rangle, \quad (2)$$

where \tilde{T}_ℓ is the Fourier transform of $T(\hat{\mathbf{n}})$ in the flat-sky approximation. The theoretical cross-spectrum $\mathcal{B}_\ell^{\text{th,ij}} \equiv \ell(\ell+1)C_\ell^{\text{th,ij}}/2\pi$ is modeled as

$$\mathcal{B}_\ell^{\text{th,ij}} = \mathcal{B}_\ell^{\text{CMB}} + \mathcal{B}_\ell^{\text{sec,ij}}, \quad (3)$$

where $\mathcal{B}_\ell^{\text{CMB}}$ is the lensed primary CMB power spectrum. In this analysis we model the secondary spectra as

$$\begin{aligned} \mathcal{B}_\ell^{\text{sec,ij}} = & \mathcal{B}_\ell^{\text{tSZ,ij}} + \mathcal{B}_\ell^{\text{kSZ,ij}} + \mathcal{B}_\ell^{\text{CIB-P,ij}} + \mathcal{B}_\ell^{\text{CIB-C,ij}} \\ & + \mathcal{B}_\ell^{\text{tSZ-CIB,ij}} + \mathcal{B}_\ell^{\text{rad,ij}} + \mathcal{B}_\ell^{\text{Gal,ij}}, \end{aligned} \quad (4)$$

with contributions from the tSZ and kSZ effects; dusty galaxies that form part of the Cosmic Infrared Background, both Poisson-like (CIB-P) and clustered (CIB-C); the cross-correlation between the tSZ effect and the CIB (tSZ-CIB); radio galaxies (rad); and dust emission from Galactic cirrus (Gal). We assume that all other cross-spectra can be neglected. Measurements by WMAP and other CMB experiments show that other Galactic emission, including synchrotron and free-free emission, is negligible in the $\nu \gtrsim 90$ GHz frequency range at these small scales and locations (e.g., Gold et al. 2011). The cross-correlation of radio sources and both tSZ and CIB sources is also expected to be small (e.g., Sehgal et al. 2010, who find a correlation of only a few per cent in simulations). Since the kSZ signal consists of positive and negative fluctuations, depending on the line-of-sight motion of the electrons that source the signal, the two-point correlation function with other signals should average to zero.

The majority of these secondary spectra will be common to all regions of the sky and to different experiments. The power in the residual radio point sources is expected, however, to vary among data sets due to the removal of bright sources. For example, for a Poisson distribution of sources with differential number counts scaling as $dN/dS \propto S^{-2}$, the Poisson power will be

$$C_\ell = \int_0^{S_{\text{max}}} S^2 \frac{dN}{dS} dS, \quad (5)$$

i.e., $C_\ell \propto S_{\text{max}}$, where S_{max} is the flux of the brightest sources in the map at a given frequency. Deeper surveys, with lower noise per pixel, are able to detect and mask out dimmer sources, so S_{max} will be lower, leading to a lower residual power. Radio sources have a shallower dN/dS slope than CIB galaxies, so imposing a flux cut of, e.g., $S_{\text{max}} = 15$ mJy removes a significant amount of radio power, but little CIB power.

The Galactic foreground power is also expected to vary between regions on the sky. The two regions mapped by ACT (Equatorial, ACT-E, and South, ACT-S) are shown in Figure 2 and summarized in Table 1, together with data from SPT. The temperature scale of the Galactic cirrus map from Finkbeiner et al. (1999) is shown for comparison. A higher level of emission is expected in some regions of the ACT-E region.

In the rest of this section we describe how each of the components in Eq. 4 are modeled. To allow for comparisons between experiments, we normalize the power spectra at a pivot frequency of $\nu_0 = 150$ GHz and scale $\ell_0 = 3000$. This differs slightly from the convention used in previous analyses of the ACT data (Fowler et al. 2010;

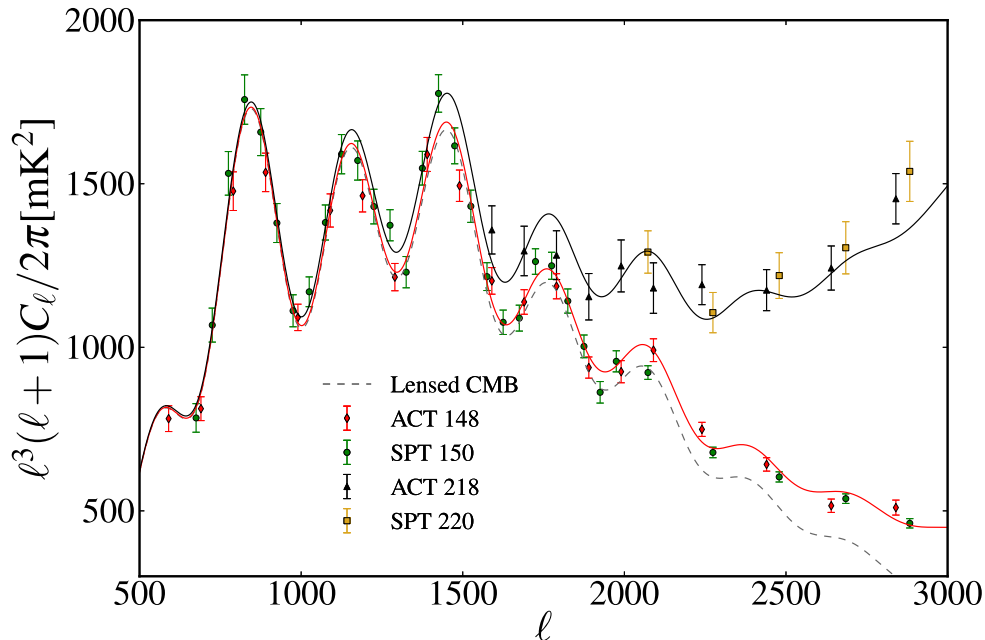


FIG. 1.— Summary of small-scale mm-wave data measured by the Atacama Cosmology Telescope (Das et al. 2013) and the South Pole Telescope (Keisler et al. 2011; Reichardt et al. 2012), in the angular range used for measuring the damping tail of the CMB. The ACT and SPT data are independently calibrated to WMAP. The vertical axis is $\ell^4 C_\ell$ instead of the conventional $\ell^2 C_\ell$ to highlight the features at these angular scales. The primary CMB signal corresponding to the best-fitting Λ CDM model (Sievers et al. 2013) is indicated (dashed), together with the total signal at 148 GHz (red, lower solid curve) and 217 GHz (black, upper solid curve), including secondary effects from SZ and foregrounds. Modeling the secondary contributions from SZ and foregrounds is vital to allow extraction of the primordial signal at small scales.

TABLE 1
SMALL-SCALE CMB DATASETS

Dataset	Frequency ^a GHz	Reference	Area sq degrees	ℓ_{\min}	ℓ_{\max}	S_c ^b mJy	ν_{tSZ}^c GHz	ν_{Rad} GHz	ν_{CIB} GHz
ACT	148	Das et al. (2013)	590 ^d	500	10000	15	146.9	147.6	149.7
	218			1500	10000		220.2	217.6	219.6
SPT-low	150	Keisler et al. (2011)	790	650	2000	50	152.9	150.2	153.8
SPT-high	95	Reichardt et al. (2012)	800	2000	9400	6.4	97.6	95.3	97.9
	150			2000	9400		152.9	150.2	153.8
	220			2000	9400		218.1	214.1	219.6

^aAll cross-spectra between channels are used in the likelihood.

^bFlux cut imposed on map by its point source mask.

^cEffective band-centers from ACT are from Swetz et al. (2011), given for tSZ, radio sources, and CIB sources.

^dThis area includes the ACT-E region at dec = 0° (300 deg²), and the ACT-S region at dec = -55° (290 deg²).

Dunkley et al. 2011). In each case we describe the parameterization used in the fiducial model; in a later section we consider possible extensions or modifications.

2.1. Thermal Sunyaev-Zel'dovich

Our model for the power from thermal SZ fluctuations is given by

$$\mathcal{B}_\ell^{\text{tSZ,ij}} = a_{\text{tSZ}} \frac{f(\nu_i)f(\nu_j)}{f^2(\nu_0)} \mathcal{B}_{0,\ell}^{\text{tSZ}}, \quad (6)$$

where $\mathcal{B}_{0,\ell}^{\text{tSZ}}$ is a template power spectrum corresponding to the predicted tSZ emission at ν_0 for a model with amplitude of matter fluctuations $\sigma_8 = 0.8$, normalized to 1 μK^2 at $\ell_0 = 3000$, and a_{tSZ} is a free parameter describing its amplitude. An example is shown

in Figure 3. The factor $f(\nu) = x \coth(x/2) - 4$, for $x = h\nu/k_B T_{\text{CMB}}$, scales the expected tSZ emission to thermodynamic units at ν , the effective band-center for the tSZ, given in Table 1. We ignore relativistic corrections (e.g., Itoh et al. 1998), since the low-mass clusters that dominate the spectra are well approximated by the non-relativistic formula. This a_{tSZ} normalization differs from that used in Dunkley et al. (2011). The present choice has the advantage of reducing the dependence on the choice of template, since the main difference between various templates is their amplitude. This means one expects to find the same constraint on a_{tSZ} regardless of template, and a constraint on the SZ power can be converted back into a model-dependent constraint on σ_8 .

The template we adopt is derived from recent hydro-

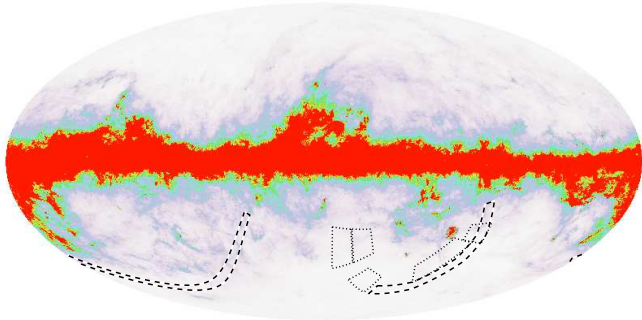


FIG. 2.— Regions of the sky used for ACT power spectra (dashed, Das et al. 2013) in the Equatorial plane (ACT-E, 300 deg²), and at -55° declination (ACT-S, 292 deg²). The 800 deg² used for SPT power spectra (dotted, Keisler et al. 2011; Reichardt et al. 2012) is indicated, with 54 deg² overlap with ACT-S. The color scales with Galactic cirrus intensity (Finkbeiner et al. 1999).

dynamic simulations described in Battaglia et al. (2012a). The simulations include the effects of radiative cooling, star formation, and feedback from AGN and supernovae. The predictions are consistent with SZ measurements from both SPT and ACT (e.g., Lueker et al. 2010), and the shape is shown in Figure 3. For the model with $\sigma_8 = 0.8$, the predicted spectrum reported in Battaglia et al. (2012a) has amplitude $a_{\text{tSZ}} = 5.6 \pm 0.9$, with standard deviation estimated from ten simulations.

Numerous other authors have also predicted the tSZ spectrum from independent simulations and analytical models (e.g., Komatsu & Seljak 2002; Shaw et al. 2009; Sehgal et al. 2010; Trac et al. 2011; Shaw et al. 2010; Battaglia et al. 2012a; Efstathiou & Migliaccio 2012), and the expected amplitude for fixed cosmological model varies depending on the astrophysical modeling of the clusters. However, the template shape is broadly consistent among models, and the data are not yet sensitive to shape difference, so we do not include a shape uncertainty. We do not mask clusters, and expect the total SZ power to be the same for ACT and SPT.

2.2. Kinematic Sunyaev-Zel’dovich

The kSZ power is expected to have contributions arising from fluctuations in the electron density (Ostriker & Vishniac 1986), and in the ionization fraction (e.g., Gruzinov & Hu 1998; McQuinn et al. 2005; Iliev et al. 2007), as well as from the motion of galaxy clusters at later times. We model the power as

$$\mathcal{B}_{\ell}^{\text{kSZ},ij} = a_{\text{kSZ}} \mathcal{B}_{0,\ell}^{\text{kSZ}}, \quad (7)$$

where $\mathcal{B}_{0,\ell}^{\text{kSZ}}$ is a template spectrum for the predicted blackbody kSZ emission for a model with $\sigma_8 = 0.8$, normalized to 1 μK^2 at $\ell_0 = 3000$. The parameter a_{kSZ} describes its normalization. We use a template that assumes a model with instantaneous reionization, described in Battaglia et al. (2010). This is derived from the same hydrodynamic simulations as the tSZ spectra in Sec 2.1, and is shown in Figure 3. The predicted amplitude from the simulations is $a_{\text{kSZ}} = 1.5$ for homogeneous reionization at $z = 10$ in a $\sigma_8 = 0.8$ cosmology. This is a quarter of the expected tSZ power. The corresponding kSZ template for the ‘nonthermal20’ model in Trac, Bode, & Ostriker (2011) has a similar ampli-

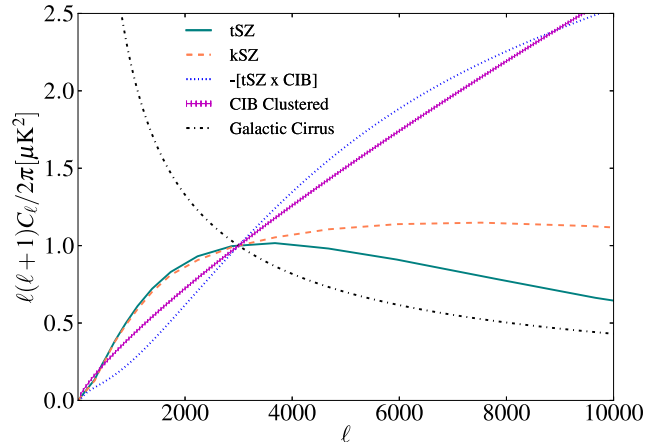


FIG. 3.— Template power spectra for the thermal and kinetic Sunyaev-Zel’dovich effects (tSZ and kSZ, Battaglia et al. 2012a, 2010), clustered CIB sources scaling as $\ell^{0.8}$ (CIB, Addison et al. 2012b), the cross-correlation between tSZ and CIB (tSZ-CIB, negative at 150 GHz, Addison et al. 2012c), and Galactic cirrus (Miville-Deschênes & Lagache 2005). They are normalized at $\ell = 3000$ and 150 GHz, and the tSZ-CIB is shown for a perfectly correlated signal. Poisson CIB and radio source power (not shown) scale as ℓ^2 .

tude and shape, as does the Shaw, Rudd, & Nagai (2012) ‘CSF’ model, and the Bode et al. (2012) model. The power is expected to scale as roughly $\sigma_8^{4.5-5}$ (Trac et al. 2011; Shaw et al. 2012)).

Reionization of the universe is not expected to be instantaneous, as was assumed by Battaglia et al. (2010). The shape and amplitude of the kSZ power from patchy reionization is far less certain, with simulations predicting a signal at least as large as the homogeneous signal (e.g., Zahn et al. 2012; Mesinger et al. 2012; Battaglia et al. 2012b). This gives a total expected signal of ~ 3 to 5 μK^2 for simple reionization models at $\ell = 3000$, comparable to the tSZ at 150 GHz. The dominant effect of patchy reionization on the power spectrum at scales probed by ACT is to alter the amplitude, depending on both the midpoint and duration of reionization (e.g., Battaglia et al. 2012b). We test a modified shape in §4.3, but do not include additional shape uncertainty in the template in the basic model.

2.3. Cosmic infrared background

Thermal dust emission from high redshift star-forming galaxies, part of the Cosmic Infrared Background (CIB), is emitted in the rest-frame far infrared and redshifted into the mm-wave range (e.g., Puget et al. 1996; Hauser et al. 1998). Clustering of these galaxies has been detected statistically in mm-wave maps at CMB frequency (Hall et al. 2010; Dunkley et al. 2011; Shirokoff et al. 2011; Planck Collaboration XVIII et al. 2011; Hajian et al. 2012; Reichardt et al. 2012), as well as in the sub-mm (e.g., Lagache et al. 2007; Viero et al. 2009). Following the analyses in Dunkley et al. (2011); Reichardt et al. (2012); Addison et al. (2012b), the power from these galaxies is modeled as the sum of a Poisson and clustered component, given by

$$\mathcal{B}_{\ell}^{\text{CIB-P},ij} = a_p \left(\frac{\ell}{\ell_0} \right)^2 \left[\frac{\mu(\nu_i, \beta_p) \mu(\nu_j, \beta_p)}{\mu^2(\nu_0, \beta_p)} \right] \mu\text{K}^2 \quad (8)$$

for the Poisson part, and

$$\mathcal{B}_\ell^{\text{CIB-C,ij}} = a_c \left(\frac{\ell}{\ell_0} \right)^{2-n} \left[\frac{\mu(\nu_i, \beta_c) \mu(\nu_j, \beta_c)}{\mu^2(\nu_0, \beta_c)} \right] \mu \text{K}^2 \quad (9)$$

for the clustered part. Here, n is a power law index, and the frequency scaling of each component is given by a modified blackbody,

$$\mu(\nu, \beta) = \nu^\beta B_\nu(T_d) g(\nu), \quad (10)$$

with emissivity indices β_p and β_c for the Poisson and clustered dust terms respectively. The function $B_\nu(T_d)$ is the Planck function at frequency ν for effective dust temperature T_d , and the function $g(\nu) = (\partial B_\nu(T)/\partial T)^{-1}|_{T_{\text{CMB}}}$ converts from flux to thermodynamic units. The parameters a_p and a_c normalize the two components at ℓ_0 and ν_0 , and different frequencies channels are assumed to be perfectly correlated.

The frequency dependence we adopt is an approximation to a sum of modified blackbodies at different redshifts, so this emissivity and temperature are only effective properties of the dust. Following Addison et al. (2012b) we fix the dust effective temperature to $T_d = 9.7$ K. We also assume $\beta_p = \beta_c$ in the basic model.

The power-law angular scaling of the clustered term, with increasing $\ell^2 C_\ell$ power at small scales, is shown in Figure 3, and approximates the shape of the non-linear power spectrum, which includes contributions from pairs of galaxies in the same dark matter halo, and between galaxies in different halos. Addison et al. (2012b) find that a power law in ℓ provides a good fit to small-scale power spectra from *Planck* and the Balloon-borne Large-Aperture Submillimeter Telescope (BLAST), and from cross-correlating ACT and BLAST maps. This is consistent with observations of the correlation function from high-redshift Lyman break galaxies, as well as local galaxies (e.g., Giavalisco et al. 1998; Connolly et al. 2002). We fix the power-law index to $n = 1.2$ in the fiducial case ($\ell^{0.8}$), in close agreement with the estimate of $n = 1.25 \pm 0.06$ in Addison et al. (2012b). Both are in agreement with galaxy correlation functions.

We do not expect the CIB power to vary significantly between the ACT and SPT maps, despite the different flux cuts applied to remove sources. Using the model in Addison et al. (2012a), the predicted effect of source masking on the CIB power is only at the per cent level.

2.4. tSZ-CIB cross-correlation

Some spatial correlation is expected between clusters that contribute to the tSZ, and CIB galaxies, since both trace the matter density field. The higher redshift and lower mass groups that make an important contribution to the tSZ signal (Komatsu & Seljak 2002; Trac et al. 2011; Battaglia et al. 2012b) are also likely to host dusty galaxies. Addison et al. (2012c) model this correlation, and predict the scale and frequency dependence of its angular power spectrum. For mm-wave spectra at $\ell > 2000$, a correlation of ~ 10 to 30% in power is predicted, with uncertainty dominated by uncertainties in the halo mass and redshift distribution of the CIB. A significant fraction of the CIB power on small scales is due to pairs of galaxies occupying group and cluster-mass halos (the ‘one-halo’ term of the halo model). These same halos are

responsible for the tSZ power. A tSZ-CIB correlation in units of power of tens of per cent is therefore possible on small angular scales even if the overall fraction of CIB emission associated with massive halos is small.

The tSZ-CIB power is negative at 150 GHz, and can partially cancel power from the kSZ effect as it does not vary significantly with frequency over the range probed by ACT and SPT. As a result, neglecting this component can lead to artificially tight constraints on the kSZ power (Zahn et al. 2012; Mesinger et al. 2012). Following Addison et al. (2012b) we model the spectrum as

$$\mathcal{B}_\ell^{\text{tSZ-CIB,ij}} = -\xi \sqrt{a_{\text{tSZ}}} a_c \frac{2f'(\nu_{ij})}{f'(\nu_0)} \mathcal{B}_{0,\ell}^{\text{tSZ-CIB}}, \quad (11)$$

where $\mathcal{B}_{0,\ell}^{\text{tSZ-CIB}}$ is the predicted correlation spectrum shape, normalized to 1 μK^2 at ℓ_0 and shown in Figure 3. The free parameter ξ is the correlation coefficient. The Poisson CIB parameter a_p is not included in Eq. 11, unlike in Shirokoff et al. (2011); Zahn et al. (2012), as the sources that dominate the CIB Poisson power in the mm-wave bands are unlikely to have significant redshift-overlap with the tSZ clusters (Addison et al. 2012c). Assuming the same modified blackbody scaling for the CIB as in §2.3, and tSZ frequency scaling $f(\nu)$, the frequency scaling of the cross-spectra in thermodynamic units is then

$$f'(\nu_{ij}) = f(\nu_i) \mu(\nu_j, \beta_c) + f(\nu_j) \mu(\nu_i, \beta_c), \quad (12)$$

for pivot scale ν_0 .

Since the correlation coefficient is poorly constrained by ACT, we impose a uniform prior of $0 < \xi < 0.2$ in the basic model; the effect of widening the range to e.g., $\xi < 0.5$, corresponding to the maximum allowed correlation in the models explored by Addison et al. (2012c), is discussed in Sievers et al. (2013). Due to the correlation between ξ and the kSZ power, broadening the limit on ξ increases the upper limit on the kSZ power, but does not affect cosmological results.

2.5. Radio point sources

The radio sources at ACT frequencies are not expected to be significantly clustered (see e.g., Sharp et al. 2010; Hall et al. 2010), and to good approximation their power should be perfectly correlated between neighbouring frequencies, consistent with simulations in Sehgal et al. (2010) and valid for sources with the same spectral indices. As in Dunkley et al. (2011) and Reichardt et al. (2012), we model the residual power after masking bright sources as Poisson scale-free power, with

$$\mathcal{B}_\ell^{\text{rad,ij}} = a_s \left(\frac{\ell}{\ell_0} \right)^2 \left(\frac{\nu_i \nu_j}{\nu_0^2} \right)^{\alpha_s} \left[\frac{g(\nu_i) g(\nu_j)}{g^2(\nu_0)} \right] \mu \text{K}^2 \quad (13)$$

in thermodynamic units, where $g(\nu)$ converts from flux units as for the CIB sources. The amplitude a_s is normalized at ν_0 and ℓ_0 . Measurements of bright sources from ACT and SPT give an estimate for the spectral index in flux units of typically $\alpha_s = -0.5$ (Vieira et al. 2010; Marriage et al. 2011). Assuming it holds at fainter fluxes, we fix $\alpha_s = -0.5$ in the fiducial model.

Bright source counts can also be used to predict a_s by extrapolating to fainter fluxes using a model for the number of sources as a function of flux. This was

done in Marriage et al. (2011) for ACT, and for SPT in Keisler et al. (2011); Reichardt et al. (2012). Using point sources measured from the full ACT dataset, Gralla et al. (2013) now predict a residual power $a_s = 2.9 \pm 0.4$ after masking sources brighter than 15 mJy in both ACT regions (the level used to construct the mask for our maps in this analysis), where the catalog is estimated to be complete. We impose this as a Gaussian prior on the power at 150 GHz. For comparison, the estimated power in the SPT power spectra after masking to a flux level of 6 mJy for SPT-high is $a_s = 1.3 \pm 0.2$ (Reichardt et al. 2012), which we also impose as a Gaussian prior.

2.6. Residual Galactic cirrus

The Galactic emission is spatially varying, and Das et al. (2013) show that dust emission can contribute significantly to the power spectra, particularly in our Equatorial region. As reported in Das et al. (2013), we apply a mask to regions of high dust emission before computing the power spectrum, using measurements at 100 μm from IRIS (Miville-Deschênes & Lagache 2005).

We then marginalize over a residual Galactic cirrus component using a power-law template

$$\mathcal{B}_\ell^{\text{Gal,ij}} = a_g \left(\frac{\ell}{\ell_0}\right)^{n_g} \left(\frac{\nu_i \nu_j}{\nu_0^2}\right)^{\beta_g} \left[\frac{g(\nu_i)g(\nu_j)}{g^2(\nu_0)}\right] \mu\text{K}^2, \quad (14)$$

with amplitude a_g , frequency index $\beta_g = 3.8$, and angular scaling $n_g = -0.7$. This angular scaling is estimated from the 100 μm IRIS dust maps (Miville-Deschênes & Lagache 2005). The frequency scaling is estimated by correlating the IRIS dust maps with ACT (Das et al. 2013), and is consistent with early results from *Planck* (Planck Collaboration XIX et al. 2011). Using the correlation coefficients estimated in Das et al. (2013), we impose priors of $a_{ge} = 0.8 \pm 0.2$, and $a_{gs} = 0.4 \pm 0.2$ in the ACT-E and ACT-S spectra respectively.

For the SPT data, a small Galactic cirrus residual is also expected. In our basic model we follow the treatment in Reichardt et al. (2012), fixing the Galactic cirrus power to $\mathcal{B}_{3000} = 0.16, 0.21,$ and $2.19 \mu\text{K}^2$ in thermodynamic units at 95, 150, and 220 GHz, with scale dependence $\propto \ell^{-1.2}$. However, this model has a steeper angular power law than in our ACT model, and a shallower frequency scaling ($\beta = 3.6$ between 150–220 GHz). For consistency we therefore test the effect of adopting the ACT model instead, using $\ell^{-0.7}$ and $\beta_g = 3.8$, and a prior of $a_g = 0.4 \pm 0.2$. We find no effect on parameters and no change in the goodness of fit.

3. FULL LIKELIHOOD FROM SMALL-SCALE DATA

In this section we describe the multi-frequency likelihood used to model the ACT data, and show how we extend it to include other small-scale datasets, in particular data from SPT.

3.1. Likelihood from the ACT data

The data from Das et al. (2013) describe the two ACT regions separately (ACT-E and ACT-S); and consist of multi-season and multi-frequency spectra, with

an associated covariance matrix¹. They are derived from ACT maps obtained using the method described in Dünner et al. (2012). The likelihood is Gaussian-distributed to good approximation. To construct the likelihood for each region, given some model spectra $C_\ell^{\text{th,ij}}$, we compute bandpower theoretical spectra using $C_b^{\text{th,ij}} = w_{b\ell}^{ij} C_\ell^{\text{th,ij}}$, where $w_{b\ell}^{ij}$ is the bandpower window function in band b for cross-spectrum ij , described in Das et al. (2013).

The likelihood, \mathcal{L} , of the data for each ACT region separately is given by

$$-2 \ln \mathcal{L} = (C_b^{\text{th}} - C_b)^T \Sigma^{-1} (C_b^{\text{th}} - C_b) + \ln \det \Sigma, \quad (15)$$

where Σ is the bandpower covariance matrix. Each of the model and data vectors C_b^{th} and C_b contain three sets of spectra,

$$C_b = [C_b^{148,148}, C_b^{148,218}, C_b^{218,218}], \quad (16)$$

for ACT-E and ACT-S separately, and each spectra set C_b^{ij} itself contains spectra for each cross-season. There are two seasons used for ACT-E (3 cross-season spectra), and three for ACT-S (6 cross-season spectra). The total likelihood is given by

$$-2 \ln \mathcal{L}_{\text{ACT}} = -2 \ln \mathcal{L}_{\text{ACT-E}} - 2 \ln \mathcal{L}_{\text{ACT-S}}. \quad (17)$$

3.1.1. Calibration and beam uncertainty

The data power spectra are calibrated, but have uncertainties. We therefore include a calibration parameter y_i , for each map i , that scales the estimated data power spectra as

$$C_b^{\text{ij}} \rightarrow y_i y_j C_b^{\text{ij}}, \quad (18)$$

and the elements of the bandpower covariance matrix as

$$\Sigma_{bb'}^{\text{ij}} \rightarrow (y_i y_j)^2 \Sigma_{bb'}^{\text{ij}}. \quad (19)$$

To account for both ACT regions, we include four calibration parameters: y_{1e}, y_{2e} for ACT-E at 148 GHz and 218 GHz, and y_{1s}, y_{2s} for ACT-S.

Das et al. (2013) calibrate the 148 GHz maps using WMAP, following the method in Hajian et al. (2011), at an effective $\ell = 700$, resulting in a 2% map calibration error in CMB temperature units. We impose this as a Gaussian prior, with $y_{1e}, y_{1s} = 1.00 \pm 0.02$. The 218 GHz maps are calibrated relative to 148 GHz, at an effective $\ell = 1500$. The 218 GHz calibration is constrained by the cross-spectrum, so no prior is imposed on y_{2e} and y_{2s} . Within each frequency, the individual seasons are calibrated to each other; the inter-season calibration error is absorbed into the single overall calibration uncertainty.

Uncertainties in the measured beam window functions for ACT at 148 GHz are between 0.7 and 0.4%, and at 218GHz between 1.5 and 0.7%. We incorporate uncertainties in the measured beams by including them directly in the covariance matrix for the spectra, described in Das et al. (2013). This technique assumes a fiducial model for the power spectra but is insensitive to its exact form.

¹ In this paper we use the original version ‘v1’ of the spectra, unless stated. Since original release, the binning and the beams have been slightly refined, generating ‘v2’ of the spectra. This is described in Das et al. (2013), and the ‘v2’ spectra are released publicly; cosmological effects are negligible as described in Sievers et al. (2013).

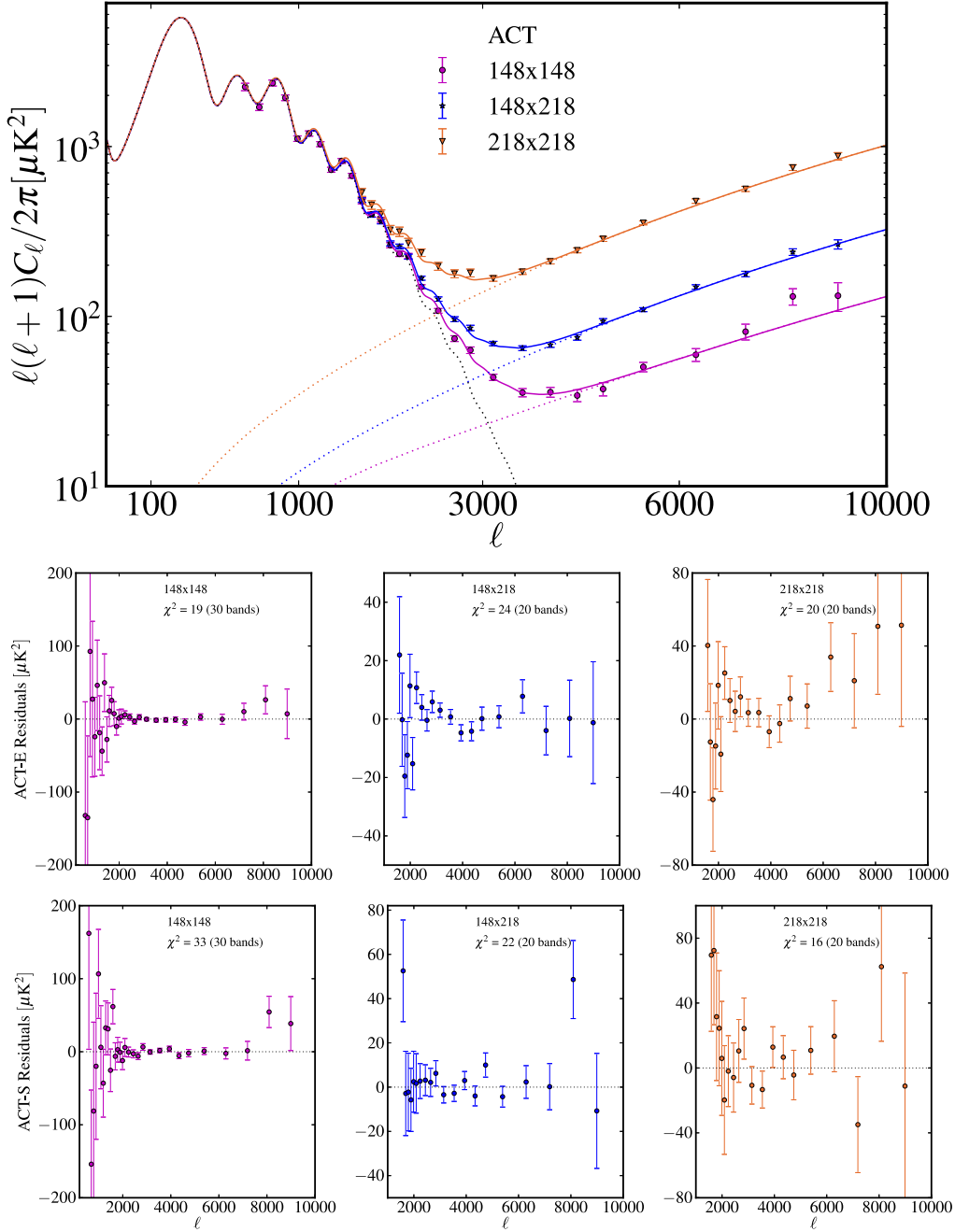


FIG. 4.— (Top) Power spectra measured by ACT (Das et al. 2013) at 148 and 218 GHz, and their cross-spectrum, coadded over ACT-E and ACT-S. We show the primary (lensed CMB in dotted black line) and secondary contributions (dotted lines) to the best-fitting model. (Bottom) Residual power in the ACT cross-frequency spectra, after subtracting the best-fitting model, at 148 GHz (left), 148x218 GHz (center), and 218 GHz (right). The errors at small scales are correlated due to beam uncertainty. The model is a good fit simultaneously to ACT-E and ACT-S, with no significant residual features.

3.1.2. Secondary model parameters

Our model described in Section 2 has nine free secondary parameters for ACT in the basic case: a_{tSZ} and a_{kSZ} describing the SZ emission, a_p , a_c and β_c describing the CIB power, a_s describing the radio power, ξ describing the tSZ-CIB cross-correlation, and a_{ge} and a_{gs} describing the Galactic cirrus emission. The latter four have strong priors imposed, as described in §2: $a_s = 2.9 \pm 0.4$, $0 < \xi < 0.2$, $a_{ge} = 0.8 \pm 0.2$, and

$a_{gs} = 0.4 \pm 0.2$. In addition to the nine model parameters, there are four calibration parameters for ACT. In §4.3 we investigate how additional, or fewer, parameters affect the fit of the model to the data. To compute the model requires an effective frequency for each component; we use the band-centers for SZ, radio, and dusty sources given in Table 1 (Swetz et al. 2011).

3.2. Combining with SPT data

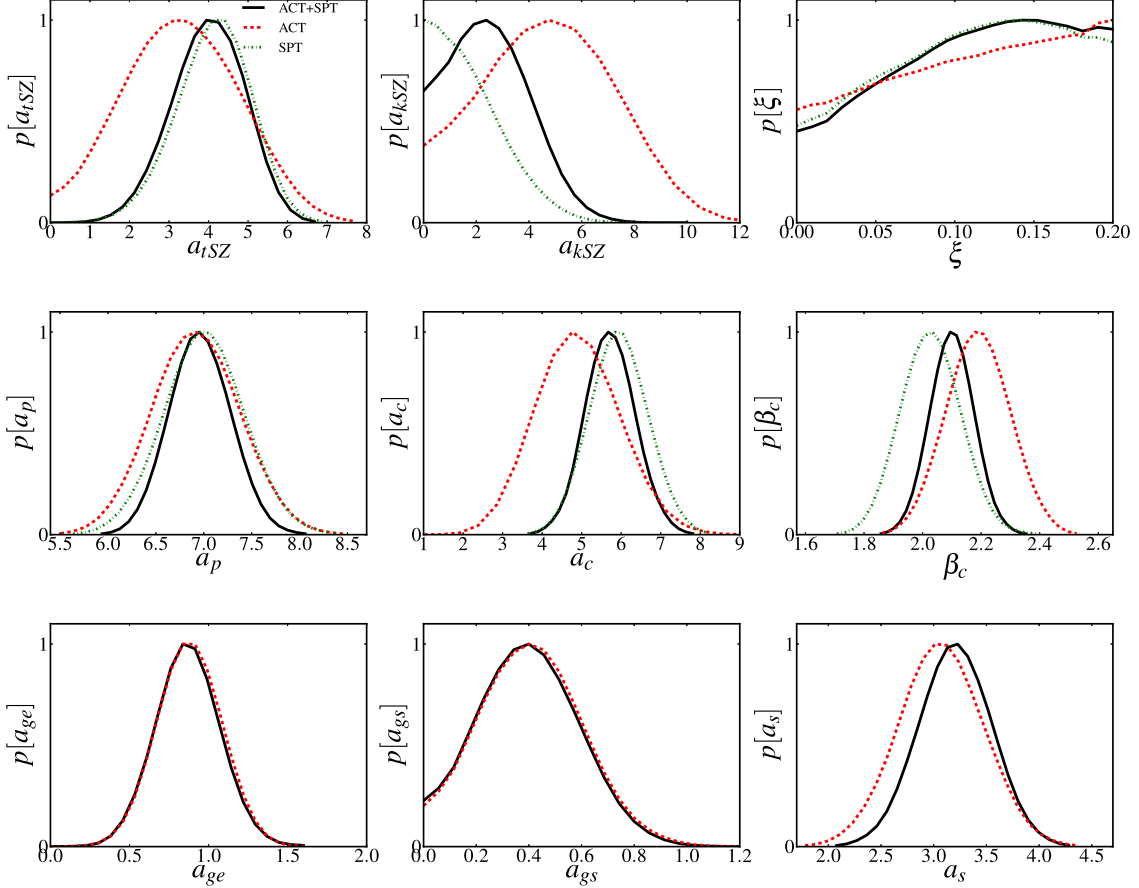


FIG. 5.— Distributions for secondary parameters from ACT and SPT, for best-fitting Λ CDM model. Parameters $\{a_{tSZ}, a_{kSZ}, a_p, a_c, a_{gs}, a_{ge}, a_s\}$ are the $\ell(\ell+1)C_\ell/2\pi$ power in μK^2 at $\ell = 3000$ and frequency 150 GHz. The tSZ-CIB correlation parameter ξ is also defined at $\ell = 3000$. The dust emissivity index β_c is in flux units, for a modified blackbody with effective temperature 9.7 K. Conversions to power at each frequency are given in Table 2. Strong priors, described in §3.1.2, are imposed on $\{\xi, a_{ge}, a_{gs}, a_s\}$.

The South Pole Telescope observed the sky from 2007–10. Spectra are reported in Keisler et al. (2011) for angular scales $650 < \ell < 3000$ at 150 GHz, and in Reichardt et al. (2012) for angular scales $2000 < \ell < 9400$ at 95, 150 and 220 GHz. These observations are summarized in Table 1. One of the goals of our work here is to test for consistency between the two experiments, by using a common framework to describe the SZ and foreground components. As this article was being prepared, refined spectra from SPT at 150 GHz were reported in Story et al. (2012); we do not include these latest data in our comparison.

Before fitting the SPT data with the ACT secondary model, we confirm that we recover the parameters and χ^2 obtained for the model used in Reichardt et al. (2012) using the SPT data. To combine the data over the full angular range, we follow the method in Reichardt et al. (2012), using the Keisler et al. (2011) data at $\ell < 2000$ (SPT-low) and the Reichardt et al. (2012) data at smaller scales (SPT-high). More radio source power has been removed from the SPT-high spectra due to masking at a deeper flux level, so the expected residual radio power in SPT-low is $\mathcal{B}_{3000} = 10.5 \pm 2.4 \mu\text{K}^2$, compared to 1.3 ± 0.2 for SPT-high. We account for this by first subtracting a radio Poisson power of $\mathcal{B}_\ell = 9.2 \mu\text{K}^2$ from the

SPT-low data, following the approach in Reichardt et al. (2012). A Gaussian prior is then imposed on the overall residual radio level in SPT of $a_{s'} = 1.3 \pm 0.2$.

We then extend the ACT secondary model to fit the SPT power spectra. Six of the ACT model parameters are expected to be common for the SPT data (the SZ and CIB parameters: $a_{tSZ}, a_{kSZ}, \xi, a_p, a_c$ and β_c). In addition, to fit the SPT data we require a separate radio source parameter, $a_{s'}$, and three calibration parameters, y_1, y_2, y_3 , to calibrate the 95, 150, and 220 GHz maps respectively. We impose a uniform prior on these calibration parameters, as the SPT covariance matrices include the calibration uncertainty.

The likelihood for ACT and SPT together is given by

$$-2 \ln \mathcal{L} = -2 \ln \mathcal{L}_{\text{ACT}} - 2 \ln \mathcal{L}_{\text{SPT}}. \quad (20)$$

The SPT likelihood is constructed as in Eq. 15, with model and data vectors

$$C_b = [C_b^{95,95}, C_b^{95,150}, C_b^{95,220}, C_b^{150,150}, C_b^{150,220}, C_b^{220,220}] \quad (21)$$

for SPT-high at $\ell > 2000$, and $C_b = C_b^{150,150}$ for SPT-low at $\ell < 2000$. To compute the model, we use the band-centers for SZ, radio and dusty sources given in Table 1, from Reichardt et al. (2012).

There is some degree of covariance between the ACT

and SPT spectra, due to the 54 deg² overlapping region of sky. Covariance between the two spectra due to cosmic variance, scaling as $1/f_{\text{sky}}$, is estimated at a level of 8% (using $54/\sqrt{590 \times 800}$); the addition of noise lowers this level, so we neglect the correlation in our combined analysis.

3.3. Multi-frequency likelihood prescription

To return the ACT (or ACT+SPT) multi-frequency likelihood for a given model we follow this approach:

- Select primary cosmological parameters, and compute a theoretical lensed CMB power spectrum $\mathcal{B}_\ell^{\text{CMB}}$ using the CAMB numerical Boltzmann code (Lewis et al. 2000).
- Select values for common secondary parameters: $\theta = \{a_{\text{tSZ}}, a_{\text{kSZ}}, \xi, a_p, a_c, \beta_c\}$.
- Select values for ACT-specific secondary and calibration parameters: $\theta = \{a_s, a_{ge}, a_{gs}, y_{1e}, y_{2e}, y_{1s}, y_{2s}\}$, and/or SPT-specific secondary and calibration parameters: $\theta = \{a_{s'}, y_1, y_2, y_3\}$.
- Compute the total theoretical secondary power spectra $\mathcal{B}_\ell^{\text{sec},ij}$ for all the required cross-spectra with Eq. 4, using the effective frequencies for each experiment.
- Compute the total model power at each frequency, $\mathcal{B}_\ell^{\text{th},ij} = \mathcal{B}_\ell^{\text{CMB}} + \mathcal{B}_\ell^{\text{sec},ij}$.
- Compute the bandpower theoretical power spectra for each dataset for both South and Equatorial regions for ACT (and for SPT), and compute the likelihood using Eq. 17.

3.3.1. Combining with WMAP

In Sievers et al. (2013) we use the ACT and SPT likelihood in combination with data from WMAP seven-year data to estimate cosmological parameters. The WMAP data measure $\ell < 1000$ angular scales, and so have minimal contamination from SZ and point sources. The public 7-year likelihood estimates the temperature spectrum from V and W bands (61 and 94 GHz, Larson et al. 2011). At these frequencies and angular scales, the infrared point source contribution is expected to be negligible, consistent with ACT and SPT measurements. The radio point source level is estimated and subtracted internally to the WMAP analysis using the multi-frequency data (e.g., Nolta et al. 2009). Finally, in light of observations by both ACT and SPT, we also neglect the SZ power in the WMAP data, as it is expected to be small: $\ell(\ell+1)C_{1000}/2\pi \sim 12 \mu\text{K}^2$ at 61 GHz from the Battaglia et al. (2012a) model, assuming $\sigma_8 = 0.8$.

4. TESTS OF THE MULTI-FREQUENCY LIKELIHOOD

In this section we test the goodness of fit of the model to the ACT power spectra, assuming the Λ CDM cosmological model. We estimate the probability distributions of the secondary parameters using the MCMC method

described in Dunkley et al. (2011), fixing the Λ CDM parameters at best-fitting values². We then investigate a set of possible extensions or modifications to the secondary model. We include the SPT power spectra and examine the consistency of the foreground model between the two datasets. We use the ACT ‘v1’ spectra for this analysis; as described earlier, a refined estimate of the beams became available after the analysis was complete. We have checked that effects on parameters are negligible ($< 0.2\sigma$), so do not update the parameter constraints or plots in this section.

4.1. ACT data

We find that the model provides a good fit to the ACT data over the full range of angular scales and frequencies. Figure 4 shows the total spectra (coadded over ACT-E and ACT-S, with the best-fitting Galactic cirrus component removed) decomposed into primary and secondary contributions. The SZ and foregrounds dominate at $\ell \gtrsim 2400$ at 218 GHz, and at $\ell \gtrsim 3200$ at 148 GHz. The goodness of fit is $\chi^2 = 675$ for 697 dof (reduced $\chi^2 = 0.98$, with PTE= 0.72, for 710 data points and 13 parameters). This indicates a good overall fit, but localised deviations can be hard to identify using the χ^2 over the full angular range. Figure 4 therefore shows the residual power after subtracting the best-fitting model; we do not observe any significant features, indicating that the model fits both the angular and frequency dependence of the data in both regions. There is a positive excess in the ACT-E residuals at the smallest scales at 218 GHz, but this is consistent with correlated beam error, accounted for in the covariance matrix.

The marginalized distributions for the secondary parameters fitting the data are shown in Figure 5 and summarized in Table 2. The Poisson-like and clustered CIB power, a_p and a_c , are detected at high significance, with index $\beta = 2.2 \pm 0.1$ consistent with Addison et al. (2012b) who find 2.20 ± 0.07 . The tSZ and kSZ power are individually seen at low significance, with an anti-correlation between a_{tSZ} and a_{kSZ} . The kSZ power peaks at a non-zero value, but the distribution is broad and consistent with zero. The total SZ power is detected at high significance. The tSZ-CIB correlation coefficient is unconstrained in the prior range $0 < \xi < 0.2$, and is also unconstrained by ACT if allowed to vary over a broader range (e.g., $\xi < 0.5$). The parameters for the power from radio sources and from Galactic cirrus are driven by their prior distributions. Sievers et al. (2013) present a physical interpretation of these parameters; the constraints are consistent with those found in the 1-year ACT analysis in Dunkley et al. (2011), with reduced errors.

In Figure 6 we show the individual components that contribute to the 148 GHz and 218 GHz power spectra after removal of the best-fitting Galactic cirrus power. At 148 GHz there are contributions from all the components. At 218 GHz the secondary spectrum is dominated by dusty point sources, both clustered and Poisson. This is illustrated further in Figure 7, which shows the frequency

² Physical baryon density $\Omega_b h^2 = 0.02226$, cold dark matter density $\Omega_c h^2 = 0.1122$, ratio of the acoustic horizon to the angular diameter distance at decoupling $\Theta = 1.040$, scalar amplitude $\ln[10^{10} A_s] = 3.186$, spectral index $n_s = 0.9707$, and optical depth $\tau = 0.898$.

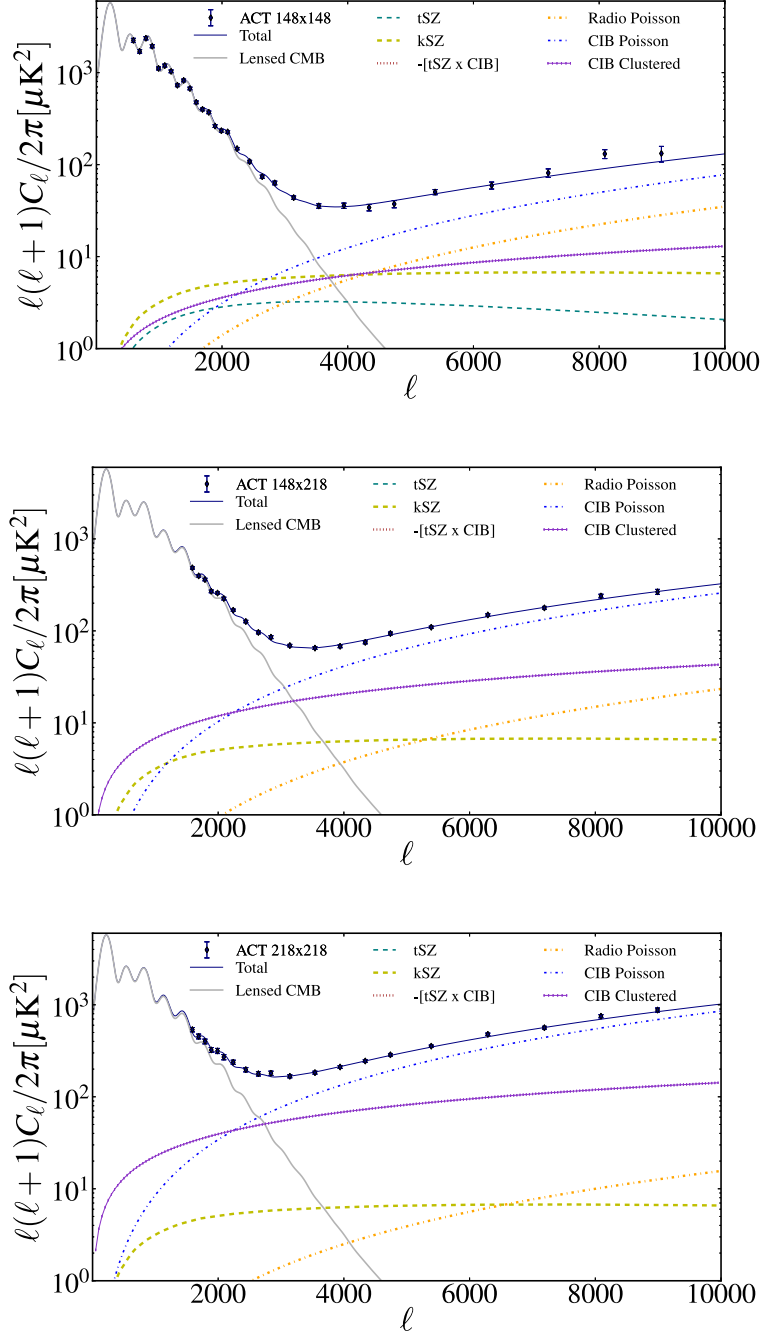


FIG. 6.— Power spectra measured by ACT at 148–218 GHz, with the best-fitting individual SZ and foreground components from Table 2. The Galactic cirrus component has been subtracted. At 148 GHz (top) the secondary components are significant at scales smaller than $\ell \sim 2000$, with contributions from tSZ, kSZ, radio galaxies, the CIB, and the tSZ-CIB correlation. The tSZ, kSZ and tSZ-CIB are non-zero in this model, but are not individually significantly detected from the ACT spectra. The radio power is constrained by bright source counts. At 218 GHz (bottom) the secondary signal is significant by $\ell \sim 1000$, and is dominated by the Poisson and clustered CIB.

dependence of the dominant components in our model at $\ell = 3000$. The derived constraints on the CIB and radio source components, and the Galactic cirrus emission, at the ACT effective frequencies are also given in Table 3 to allow comparison with other models.

4.2. Combination with SPT

The same model also provides a good fit to the SPT spectra. The SPT data extend the frequency range to

95 GHz, adding three additional cross-spectra to the likelihood. We show the parameters estimated from SPT alone in Figure 5 and in Table 2; they are consistent with those from ACT, with $\sim 1\sigma$ shifts in a_{kSZ} and β_c . The radio Poisson level is lower due to the greater number of radio sources masked in the SPT maps. The model is shown with the SPT spectra in Figure 8; the goodness of fit is $\chi^2 = 96$ for 107 dof (reduced $\chi^2 = 0.89$, PTE=0.77).

TABLE 2
 LIKELIHOOD PARAMETERS, ASSUMING BEST-FIT 6-PARAMETER Λ CDM FOR THE LENSED CMB^a.

	Parameter	Prior ^b	ACT ^c	SPT	ACT+SPT
SZ	a_{tSZ}	> 0	3.3 ± 1.4	4.1 ± 0.9	4.0 ± 0.9
	a_{kSZ}	> 0	< 8.6	< 4.2	$< 5.0^{\text{d}}$
CIB	a_p	> 0	6.9 ± 0.4	7.0 ± 0.4	7.0 ± 0.3
	a_c	> 0	4.9 ± 0.9	6.0 ± 0.7	5.7 ± 0.6
	β_c	> 0	2.2 ± 0.1	2.0 ± 0.1	2.10 ± 0.07
tSZ-CIB	ξ	$0 < \xi < 0.2$	< 0.2	< 0.2	< 0.2
Radio	a_s	2.9 ± 0.4	3.1 ± 0.4	—	3.2 ± 0.3
	$a_{s'}$	1.3 ± 0.2	—	1.4 ± 0.1	1.4 ± 0.1
Galactic cirrus ^e	a_{ge}	0.8 ± 0.2	0.9 ± 0.2	—	0.9 ± 0.2
	a_{gs}	0.4 ± 0.2	< 0.73	—	< 0.70
Calibration	y_{1e}	1.00 ± 0.02	1.010 ± 0.007	—	1.006 ± 0.006
	y_{2e}	—	0.99 ± 0.01	—	0.99 ± 0.01
	y_{1s}	1.00 ± 0.02	1.011 ± 0.007	—	1.010 ± 0.007
	y_{2s}	—	1.03 ± 0.01	—	1.02 ± 0.01
	y_1	—	—	1.01 ± 0.02	1.01 ± 0.02
	y_2	—	—	1.007 ± 0.008	1.008 ± 0.008
	y_3	—	—	1.02 ± 0.02	1.03 ± 0.02
best fit χ^2/dof			675/697	96/107	773/810
PTE			0.72	0.77	0.82

^aSecondary parameters marginalized over the 6 Λ CDM model parameters are reported in Table 1 of Sievers et al. (2013), and are consistent with these results. The marginalization has little effect on these secondary parameters, increasing errors by at most 10%.

^bA flat prior is imposed, unless indicated as a Gaussian with $x \pm y$ for mean x and standard deviation y .

^cResults are reported as 68% confidence levels or 95% upper limits; ξ is unconstrained so the prior upper limit is reported.

^dIf the prior on ξ is broadened to $0 < \xi < 0.5$, the upper limit increases to $a_{\text{kSZ}} < 6.9$ (Sievers et al. 2013).

^eThe SPT cirrus level we use is $\mathcal{B}_{3000} = 0.16, 0.21, \text{ and } 2.19 \mu\text{K}^2$ at 95, 150, and 220 GHz, as measured in Reichardt et al. (2012).

 TABLE 3
 DERIVED CONSTRAINTS ON FOREGROUND POWER, \mathcal{B}_{3000} (μK^2)

	ACT		SPT		
	148 GHz	218 GHz	95 GHz	150 GHz	220GHz
CIB-P	6.8 ± 0.4	78 ± 12	0.90 ± 0.02	8.0 ± 0.5	69 ± 10
CIB-C	4.8 ± 0.9	54 ± 16	0.76 ± 0.02	6.8 ± 0.8	59 ± 12
Radio	3.2 ± 0.4	1.4 ± 0.2	7.2 ± 0.8	1.4 ± 0.2	0.7 ± 0.1
Gal-E ^a	0.9 ± 0.2	11 ± 2.3			
Gal-S	0.4 ± 0.2	5.0 ± 2.3			

^aGal-E and Gal-S are the Galactic cirrus powers in the ACT-E and ACT-S spectra. The levels are close to the priors imposed from the measured cross-correlations with IRIS (Das et al. 2013)

Given the consistency of the two datasets, we combine them to generate a joint likelihood; Figure 5 includes the secondary parameters derived from a joint fit. In this case there are ten foreground parameters, and seven calibration parameters. The tenth foreground parameter (not plotted) is $a_{s'}$ for the Poisson radio sources in SPT. The goodness of fit of the joint model is $\chi^2 = 773$, which can be compared to $\chi^2 = 675 + 96 = 771$ for the independent fit to each data set. This supports their consistency.

We report the derived constraints on the CIB and radio source components at the ACT and SPT effective frequencies for each band in Table 3. A difference of approximately 15% is expected between the CIB power at 148 GHz for ACT and 150 GHz for SPT, due to different effective bandpass frequencies and the strong CIB

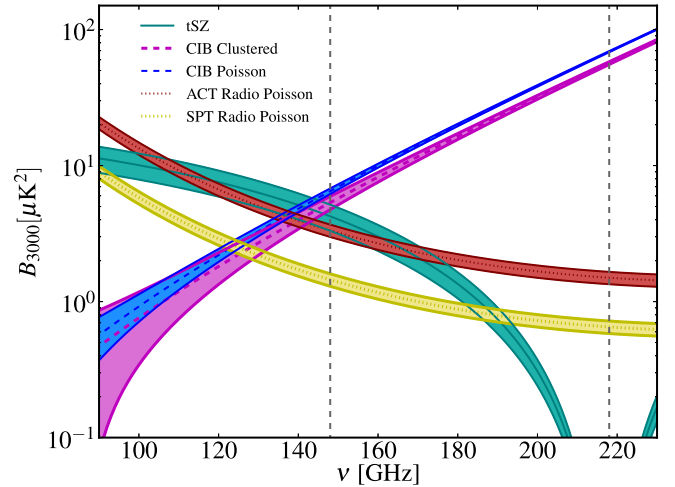


FIG. 7.— Frequency dependence of the dominant components of the foreground power at $\ell = 3000$ measured by the combined ACT and SPT data sets. The bands show the 1σ uncertainties from Table 2. At 150 – 220 GHz the power from fluctuations in the CIB dominates; at lower frequencies the thermal SZ and radio source power is more significant. The SPT radio power is lower due to deeper integration. The kSZ and tSZ-CIB components are not shown.

frequency dependence across the mm-wave bands.

4.3. Tests of the likelihood

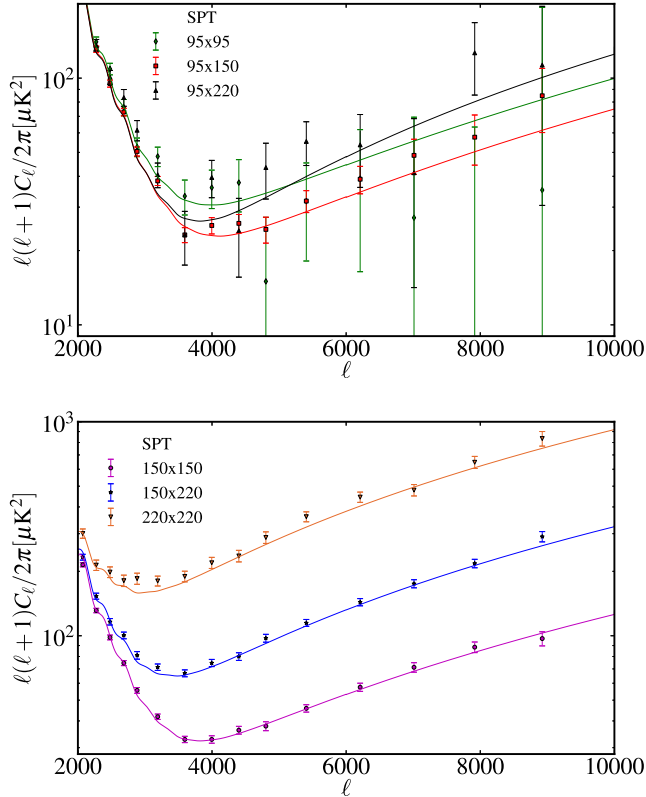


FIG. 8.— Power spectra at 95, 150 and 220 GHz, and their cross-spectra, measured by SPT (Reichardt et al. 2012), fit with the same model as the ACT data in Figure 4. At 150 GHz the SPT-low spectrum from Keisler et al. (2011) is included, with excess radio power subtracted for comparison. Accounting for the different flux cuts applied to the ACT and SPT maps, and the different bandpass effective frequencies, the spectra are consistent.

TABLE 4
MODIFICATIONS TO SECONDARY MODEL

Model	Number of parameters ^a	ACT ^b $\Delta\chi^2$
Fiducial	9	0
CIB index n free	10	-4
$\beta_c \neq \beta_p$	10	0
CIB Poisson corr = 0.8	9	5
CIB Clustered corr = 0.8	9	1
CIB $T_d = 13.6$ K	9	1
Fixed kSZ, $a_{\text{kSZ}} = 1.5$	8	3
Altered kSZ shape	9	1
No tSZ-CIB corr, $\xi = 0$	8	2
No SZ	6	21
Radio index $\alpha_s = 0$	9	1
No Galactic residual	7	6

^aDoes not include calibration parameters.

^bWe report the $\Delta\chi^2$ to the nearest integer.

This model fits the ACT and SPT data, and includes our uncertainties about the physical components, with priors describing our knowledge from other observations. However, it is a simplified parameterization of the emission. We therefore consider a set of extensions or modifications to the model, and test how the goodness of fit to the ACT data is affected by an increase or decrease in parameters, or a change in the prior assumptions. In these tests, summarized in Table 4, we hold the cosmological model fixed at the best-fitting Λ CDM parameters. A subset of these extensions are considered further in Sievers et al. (2013), testing their effect on the primary cosmological parameters.

The CIB appears to be well-fit currently by a power-law in angular scale, with $\mathcal{B}_\ell \propto \ell^{0.8}$. Addison et al. (2012b) find an uncertainty of 0.06 in this scaling. If we allow the index n to vary, we find no improvement in the fit, but parameter distributions for the CIB parameters a_p and a_c are broadened, as they are correlated with the power-law scaling. We also assume that the CIB emission is perfectly correlated among frequencies, in the range 95–220 GHz. Evidence for imperfect correlation was reported in Planck Collaboration XVIII et al. (2011). The effect of this assumption is tested by setting the correlation coefficient to < 1 in the model, choosing 0.8 for either the Poisson or clustered components, roughly corresponding to the degree of correlation between maps reported in Planck Collaboration XVIII et al. (2011). For the Poisson component we find that this degrades the goodness of fit by $\Delta\chi^2 = 5$ compared to the perfectly correlated case. We also assume a common frequency scaling of the clustered and Poisson terms. A different scaling in frequency may be expected if, for instance, the redshift dependence of the clustered and Poisson power is different, so a common index is not necessarily expected. Allowing it to vary independently does not significantly improve the goodness of fit, but does lead to a poorly constrained distribution for β_c , and removes the detection of the CIB at 148 GHz. The index for the Poisson sources in this case, $\beta_p = 2.14 \pm 0.15$, is consistent with the joint index. Changing the effective dust temperature from 9.7 K to 14 K, consistent with the value obtained by Gispert et al. (2000) from a fit to the FIRAS CIB frequency spectrum, has no effect on the model, apart from a corresponding change in β_c .

Exploring the SZ assumptions, we consider fixing the kSZ contribution to the linear theory estimate for a universe with $\sigma_8 = 0.8$, assuming homogeneous reionization. This degrades the goodness of fit of the model by only $\Delta\chi^2 = 3$, indicating that the data cannot yet distinguish between homogeneous and patchy reionization. Limiting the kSZ in this way also leads to tighter constraints on the tSZ power. Modifying instead the shape, we find that adding a patchy reionization template from Battaglia et al. (2012b) to the kSZ, which changes its shape, does not affect the other secondary parameters. Neglecting the tSZ-CIB cross-correlation also fits the data equally well for one fewer parameter. The dependence of the kSZ constraints on the model for the tSZ-CIB correlation is explored further in Sievers et al. (2013). If we neglect the SZ components altogether, setting $a_{\text{tSZ}} = a_{\text{kSZ}} = 0$ and keeping only the CIB and Galactic components, the goodness of fit significantly worsens, with an increase of $\Delta\chi^2 = 21$.

Our model imposes an *a priori* assumption on the frequency scaling of the extragalactic radio sources. We test the effect of changing the radio spectral index to $\alpha_s = 0$, finding negligible effect on parameters and goodness of fit. There is also little effect from changing the prior on the power from Gralla et al. (2013) by 1σ , corresponding to a different model for the bright radio sources that lie above the detection threshold. Removing the prior altogether opens up degeneracies with other parameters, but does not significantly improve the goodness of fit.

Finally, we test the effect of removing the Galactic cirrus components; the goodness of fit worsens by $\Delta\chi^2 = 6$ and the clustered CIB level increases. This indicates a preference for Galactic cirrus at the 95% confidence level.

5. CMB-ONLY LIKELIHOOD

Understanding the contribution of the secondary components to the ACT power spectra is vital for extracting the cosmological information, due to possible degeneracies between primary and secondary parameters. Values of the secondary parameters are also astrophysically interesting. However, if we are only interested in the cosmological parameters, a simplified likelihood is desirable.

We construct a CMB-only likelihood from ACT data as follows. Instead of using the ACT likelihood to estimate cosmological parameters, we take the intermediate step of estimating the CMB power spectrum in bandpowers, marginalizing over the possible contamination. This is a natural extension to forms of CMB data compression that have been adopted in earlier analyses (e.g., Bond, Jaffe, & Knox 2000). Such ‘grand unified spectra’ were used in a number of subsequent papers to combine the results from various CMB experiments, marginalizing over a variety of nuisance parameters, e.g., in Sievers et al. (2003); Bond et al. (2003); Bond et al. (2004). At large scales, where contamination from SZ and point sources is negligible, the estimated CMB is simply an optimally combined average of the multi-frequency spectra as in e.g., Hinshaw et al. (2003). At smaller scales the CMB spectrum has additional uncertainty due to secondary contamination.

By marginalizing over nuisance parameters in the spectrum-estimation step, we can effectively decouple the primary CMB from non-CMB information. No additional nuisance parameters are then needed when estimating cosmological parameters.

5.1. Method: bandpowers via Gibbs sampling

To implement this method in practice, we estimate n_b CMB bandpowers, marginalizing over the secondary parameters. We use the full multi-frequency likelihood from §3 to do this, but estimate CMB bandpowers instead of cosmological parameters.

We recall that the model for the theoretical power for a single cross-frequency, cross-season spectrum, $C_\ell^{\text{th},ij}$, is written as

$$C_\ell^{\text{th},ij} = C_\ell^{\text{CMB}} + C_\ell^{\text{sec},ij}(\theta), \quad (22)$$

where $C_\ell^{\text{sec},ij}(\theta)$ is the secondary signal as in Eq. 4, and is a function of secondary parameters θ . Writing the spectrum in bandpowers, $C_b^{\text{th},ij} = w_{b\ell}^{ij} C_\ell^{\text{th},ij}$, where w are the bandpower window functions, we write the model for

the bandpowers in vector form as

$$C_b^{\text{th}} = \mathbf{A}C_b^{\text{CMB}} + C_b^{\text{sec}}(\theta), \quad (23)$$

where C_b^{th} and C_b^{sec} are multi-frequency, multi-season vectors of length $n_b \times n_{\text{spec}}$, where n_b is the number of bandpowers, and n_{spec} is the number of cross-season and cross-frequency spectra ($n_{\text{spec}} = 9$ for ACT-E, and 18 for ACT-S). The secondary spectra differ between frequencies but not between seasons. The mapping matrix \mathbf{A} , with elements that are either 1 or 0, maps the CMB bandpower vector (of length n_b), which is the same at all frequencies and in all seasons, onto the $(n_b \times n_{\text{spec}})$ -length data vector.

We want to estimate C_b^{CMB} , marginalized over the secondary parameters, θ . The posterior distribution for C_b^{CMB} , given the observed multi-frequency, multi-season spectra C_b , can be written as

$$p(C_b^{\text{CMB}}|C_b) = \int p(C_b^{\text{CMB}}, \theta|C_b)p(\theta)d\theta. \quad (24)$$

We find that Gibbs sampling provides an efficient way to map out the joint distribution $p(C_b^{\text{CMB}}, \theta|C_b)$, and to extract the desired marginalized distribution $p(C_b^{\text{CMB}}|C_b)$.

Gibbs sampling can be used in the special case that at least one conditional slice through a multi-dimensional distribution has a known form, and has been used, for example, to estimate the large-scale CMB power spectrum, and to marginalize over Galactic foregrounds (e.g., Wandelt et al. 2004; Jewell et al. 2004; Eriksen et al. 2004; Dunkley et al. 2009; Larson et al. 2011). Here, we split the joint distribution into two conditional distributions: $p(C_b^{\text{CMB}}|\theta, C_b)$, and $p(\theta|C_b^{\text{CMB}}, C_b)$. We write the multi-frequency likelihood for a single ACT region, from Eq. 15, as

$$-2 \ln \mathcal{L} = (\mathbf{A}C_b^{\text{CMB}} + C_b^{\text{sec}} - C_b)^T \boldsymbol{\Sigma}^{-1} (\mathbf{A}C_b^{\text{CMB}} + C_b^{\text{sec}} - C_b) + \ln \det \boldsymbol{\Sigma}, \quad (25)$$

which is a multivariate Gaussian.

If C_b^{sec} is held fixed, the conditional distribution for the CMB bandpowers, $p(C_b^{\text{CMB}}|\theta, C_b)$, assuming a uniform prior for $p(C_b^{\text{CMB}})$, is then also a Gaussian. It has a distribution given by

$$-2 \ln p(C_b^{\text{CMB}}|\theta, C_b) = (C_b^{\text{CMB}} - \hat{C}_b)^T \mathbf{Q}^{-1} (C_b^{\text{CMB}} - \hat{C}_b) + \ln \det \mathbf{Q}, \quad (26)$$

The mean, \hat{C}_b , and covariance, \mathbf{Q} , of this conditional distribution are obtained by taking the derivatives of the likelihood in Eq. 25 with respect to C_b^{CMB} . This gives mean

$$\hat{C}_b = [\mathbf{A}^T \boldsymbol{\Sigma}^{-1} \mathbf{A}]^{-1} [\mathbf{A}^T \boldsymbol{\Sigma}^{-1} (C_b - C_b^{\text{sec}})], \quad (27)$$

and covariance

$$\mathbf{Q} = \mathbf{A}^T \boldsymbol{\Sigma}^{-1} \mathbf{A}. \quad (28)$$

We can draw a random sample from this Gaussian distribution by taking the Cholesky decomposition of the covariance matrix, $\mathbf{Q} = \mathbf{L}\mathbf{L}^T$, and drawing a vector of Gaussian random variates G . The sample is then given by $C_b^{\text{CMB}} = \hat{C}_b + \mathbf{L}G$.

If instead C_b^{CMB} is held fixed, the conditional distribution for the secondary parameters, $p(\theta|C_b^{\text{CMB}}, C_b)$, is

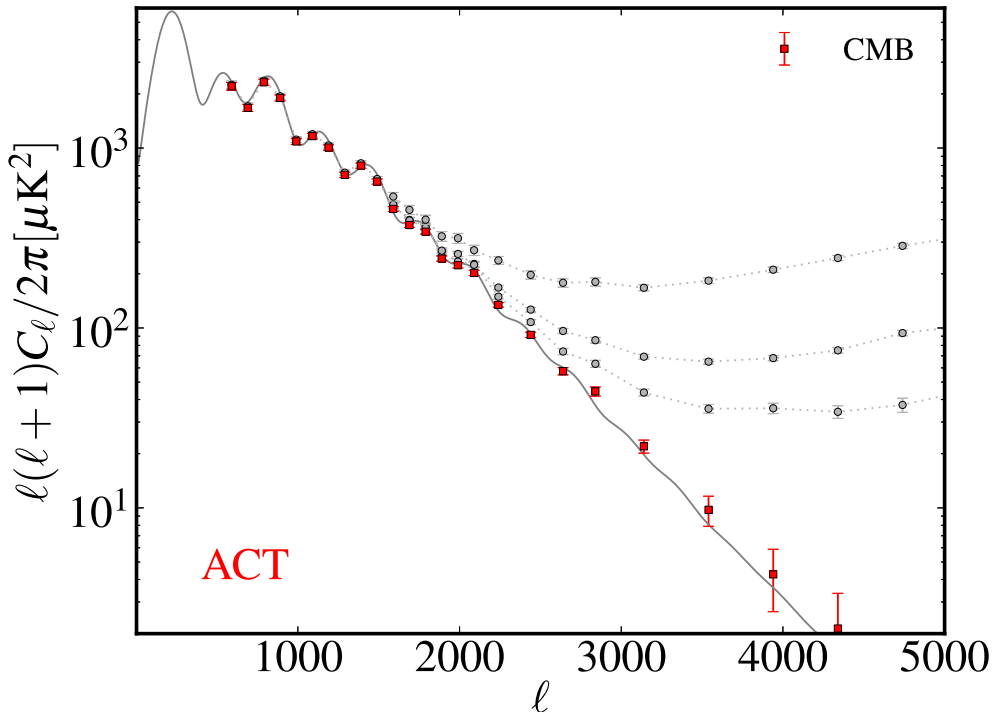


FIG. 9.— Estimated CMB bandpowers from ACT, marginalized over extragalactic source and SZ components. Bandpowers are estimated for ACT-E and ACT-S separately; here we show the inverse-variance weighted combination. The bandpowers are correlated at the $\sim 20\%$ level at scales $\ell \gtrsim 2000$ due to covariance with the secondary parameters. The total multi-frequency spectra for ACT-E (dashed, at 148 GHz, 148×218 GHz, and 218 GHz) are also shown to indicate the significant level of SZ and foreground power at small scales.

not a Gaussian, but can be sampled with the Metropolis algorithm that is used in the MCMC sampling in §4. To map out the full joint distribution for θ and C_b^{CMB} we alternate a Gibbs sampling step, drawing a new vector of CMB bandpowers, C_b^{CMB} , with a Metropolis step, drawing a trial vector of the secondary parameters θ .

We choose a uniform positive prior distribution for $p(C_b^{\text{CMB}})$, and restrict the CMB bandpowers to be zero at $\ell > 4500$, where the CMB power is expected to be less than $1 \mu\text{K}^2$. About 100,000 steps are required for convergence of the joint distribution, assessed with the Dunkley et al. (2005) spectral test. The mean and covariance of the resulting marginalized bandpowers, C_b^{CMB} , are then estimated following the standard MCMC prescription (e.g., Lewis & Bridle 2002; Spergel et al. 2003).

5.1.1. Combining spectra from different regions

There is only one underlying CMB power spectrum, so this method could be used to estimate a single spectrum, or set of bandpowers, from the two ACT regions. However, the bandpower window functions are different for each region due to their distinct geometries. To easily conserve this information, we estimate the CMB bandpowers for ACT-E and ACT-S separately. Since the secondary parameters are common to both, the estimated CMB bandpowers will be correlated between the regions at small scales.

To estimate the joint distribution for the ACT-E and ACT-S bandpowers, we map out $p(C_b^{\text{CMB-E}}, C_b^{\text{CMB-S}}, \theta | C_b)$ by taking sequential sam-

pling steps from the conditional distributions:

$$\begin{aligned} & p(C_b^{\text{CMB-E}} | C_b^{\text{CMB-S}}, \theta, C_b), \\ & p(C_b^{\text{CMB-S}} | C_b^{\text{CMB-E}}, \theta, C_b), \\ & p(\theta | C_b^{\text{CMB-E}}, C_b^{\text{CMB-S}}, C_b). \end{aligned} \quad (29)$$

The marginalized distribution for the CMB bandpowers, $p(C_b^{\text{CMB-E}}, C_b^{\text{CMB-S}} | C_b)$, with its associated covariance matrix, is then computed from the samples. This could be extended to include the SPT data, or data from *Planck*, for example.

5.1.2. Calibration factors

There are four ACT calibration factors. To minimize bin-to-bin correlations in the estimated CMB bandpowers due to calibration uncertainty, we divide out the 148 GHz calibrations for the two ACT spectra, estimating $C_b^{\text{CMB-E}} = C_b^{\text{CMB-E}}/y_{1e}^2$ for the ACT-E bandpowers, and $C_b^{\text{CMB-S}} = C_b^{\text{CMB-S}}/y_{1s}^2$ for ACT-S.

We then estimate the 148 GHz calibration factors, y_{1e} , y_{1s} , and relative 218/148 GHz calibration factors, y_{2e}/y_{1e} , y_{2s}/y_{1s} , as part of the secondary parameter set.

5.2. Marginalized CMB bandpowers

Figure 9 shows the estimated CMB bandpowers from the ACT-E and ACT-S spectra, co-added together and compared to the multi-frequency spectra. The bandpowers for each region are reported in Table 5. In this table we report the CMB spectra derived using the updated ‘v2’ multi-frequency spectra. Without assuming any cosmological model, the CMB bandpowers over the full an-

gular range are remarkably consistent with the theoretical Λ CDM model predicted by WMAP. The uncertainty on the bandpowers rises at scales smaller than $\ell \sim 3000$, and the correlations between bandpowers increases.

Figure 10 shows the effect of marginalization on the bandpower errors, using the ratio between the marginalized errors and the unmarginalized errors for a fixed secondary model. It is clear that by measuring the spectrum at multiple frequencies, the CMB can be successfully separated from secondary contamination out to scales $\ell \lesssim 3500$. At scales $\ell < 2000$ there is little error inflation due to foreground uncertainty, and the errors are inflated by $\sim 20\%$ (15%) by $\ell = 3200$ for the ACT-E (ACT-S) spectra. The marginalized distributions for the CMB bandpowers are well approximated by Gaussians for multipoles to band-center $\ell = 3540$ for ACT, as shown in the Appendix.

We compare the secondary parameters recovered in this model-independent sampling to the case where Λ CDM is assumed. This comparison is shown in the Appendix; the parameters are consistent, with about a 1σ shift in the estimated kSZ power. We find that the CMB bandpowers are not strongly correlated with the secondary parameters until scales well into the Silk damping tail at $\ell \gtrsim 2500$; a dominant correlation is then with the kSZ power due to its blackbody frequency dependence, and a smaller kSZ power – compensated by larger primary CMB power – is allowed when the Λ CDM assumption is relaxed. The CMB bandpower covariance matrix conserves this correlation information.

TABLE 5
LENSED CMB ANISOTROPY POWER^a

ℓ_b	$\ell(\ell+1)C_b/2\pi$ (μK^2)		Coadd ^b
	ACT-E	ACT-S	
590	2157 \pm 159	2343 \pm 160	2250 \pm 113
690	1729 \pm 115	1744 \pm 107	1737 \pm 78
790	2499 \pm 146	2274 \pm 126	2370 \pm 96
890	1945 \pm 109	1903 \pm 102	1923 \pm 74
990	1068 \pm 58	1187 \pm 61	1124 \pm 42
1090	1206 \pm 61	1149 \pm 58	1176 \pm 42
1190	1036 \pm 51	1016 \pm 48	1026 \pm 35
1290	679 \pm 33	766 \pm 38	717 \pm 25
1390	819 \pm 39	787 \pm 36	802 \pm 26
1490	661 \pm 31	650 \pm 29	655 \pm 21
1590	452 \pm 19	474 \pm 21	462 \pm 14
1690	387 \pm 16	355 \pm 17	372 \pm 11
1790	344 \pm 14	347 \pm 16	345 \pm 10
1890	242 \pm 10	246 \pm 12	244 \pm 8
1990	230 \pm 10	214 \pm 11	223 \pm 8
2090	199 \pm 9	204 \pm 11	201 \pm 7
2240	137 \pm 5	127 \pm 6	133 \pm 4
2440	92.9 \pm 3.9	87.8 \pm 5.1	91.0 \pm 3.1
2640	57.6 \pm 3.3	56.4 \pm 4.5	57.2 \pm 2.6
2840	43.0 \pm 3.2	44.7 \pm 4.2	43.6 \pm 2.5
3140	22.5 \pm 2.2	19.3 \pm 2.8	21.3 \pm 1.7
3540	9.2 \pm 2.3	9.0 \pm 2.8	9.1 \pm 1.8

^aTo compute a likelihood using these data, ACT-E and ACT-S should be used with the covariance matrix and bandpower window functions provided on LAMBDA.

^bThis coadds the ACT-E and ACT-S CMB bandpowers for plotting purposes.

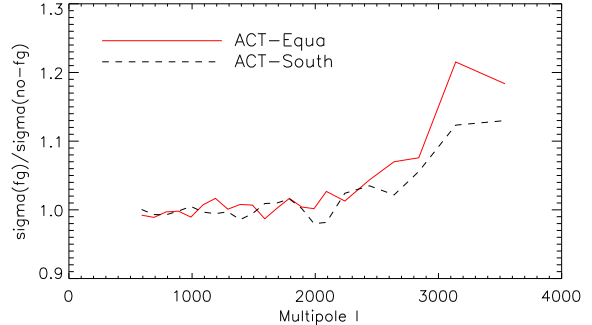


FIG. 10.— Inflation of errors due to foreground marginalization, relative to the errors for a best-fitting foreground model: at scales smaller than $\ell \sim 2000$, the errors are increased due to foreground uncertainty.

5.3. The CMB-only likelihood

We construct the CMB-only likelihood from the angular range where the CMB bandpowers are Gaussian, conservatively choosing $\ell < 3500$. We do not use the $3500 < \ell < 4500$ bandpowers as they are increasingly non-Gaussian, due to the foreground marginalization, and are more strongly correlated with foreground parameters. The likelihood is given by

$$-2 \ln \mathcal{L}(\tilde{C}_b^{\text{CMB}} | C_\ell^{\text{th}}) = x^T \tilde{\Sigma}^{-1} x + \ln \det \tilde{\Sigma}. \quad (30)$$

Here

$$x = \begin{pmatrix} \tilde{C}_b^{\text{CMB-E}} - w_{b\ell, \text{ACT-E}} C_\ell^{\text{th}} \\ \tilde{C}_b^{\text{CMB-S}} - w_{b\ell, \text{ACT-S}} C_\ell^{\text{th}} \end{pmatrix}, \quad (31)$$

where \tilde{C}_b^{CMB} and $\tilde{\Sigma}$ are the marginalized mean and covariance matrix for the bandpowers, and C_ℓ^{th} is the lensed CMB spectrum generated from e.g., CAMB. We use 21 bandpowers for ACT-E and ACT-S in the range $500 < \ell < 3500$. A single calibration parameter for each region is marginalized over analytically, following Bridle et al. (2002). The prescription for using this likelihood is simple, as no extra nuisance parameters are needed.

To test the performance of this compressed likelihood, results are compared using the full multi-frequency likelihood, and the CMB-only likelihood. Cosmological parameters are estimated for the restricted Λ CDM 6-parameter model, and a set of more extended models that probe the damping tail and peak shapes, including the running of the spectral index, the number of relativistic degrees of freedom N_{eff} , the lensing amplitude A_L , and the variation in fine structure constant, α . Parameter constraints using both likelihoods agree to 0.1σ , and are reported in Sievers et al. (2013). We conclude that this is an efficient alternative to the full likelihood for the typical extensions considered in cosmological analyses, although the full likelihood may give more optimal results for unusual models with features far into the damping tail.

6. SUMMARY

In this paper we have presented a likelihood formalism to describe the ACT multi-frequency power spectra that includes contributions from SZ and foreground components in addition to the lensed CMB. We model the data including four late-time astrophysical components:

thermal and kinetic SZ, emission from CIB galaxies, and emission from radio galaxies.

We have quantified these components using seven power spectra, splitting the CIB into a Poisson and clustered part, and including power from the cross-correlation between tSZ emission from clusters, and emission from CIB galaxies that also trace the large scale structure. Rather than a minimal model with the fewest parameters, we have sought a model that includes our uncertainties with priors describing our knowledge from additional observations. For example, while the data do not demand that we include the tSZ-CIB correlation, we are motivated to include it to avoid placing unphysically strong limits on the kSZ power.

Modeling these astrophysical components allows us to probe the primordial CMB fluctuations down to an angular resolution of $4'$ using ACT. We have used the model to extract an estimate of the primordial CMB spectrum well into the Silk damping tail, marginalizing over the foreground uncertainty. This produces a simplified compressed likelihood for use in cosmological parameter estimation.

We find that data observed by the South Pole Telescope give results consistent with ACT, accounting for the different removal of radio point sources, and different degree of contamination by Galactic cirrus. SPT and ACT have very different instrument design and scan strategies, and their observations on the sky have limited

overlap. The excellent agreement between the datasets is not only an important cross-check but is another demonstration of cosmic homogeneity.

This work was supported by the U.S. National Science Foundation through awards AST-0408698 and AST-0965625 for the ACT project, as well as awards PHY-0855887 and PHY-1214379. Funding was also provided by Princeton University, the University of Pennsylvania, and a Canada Foundation for Innovation (CFI) award to UBC. ACT operates in the Parque Astronómico Atacama in northern Chile under the auspices of the Comisión Nacional de Investigación Científica y Tecnológica de Chile (CONICYT). Computations were performed on the GPC supercomputer at the SciNet HPC Consortium. SciNet is funded by the CFI under the auspices of Compute Canada, the Government of Ontario, the Ontario Research Fund – Research Excellence; and the University of Toronto. Funding from ERC grant 259505 supports JD, EC, and TL. We thank George Efstathiou and Steven Gratton for useful discussions, and Christian Reichardt for help with the SPT data. We acknowledge the use of the Legacy Archive for Microwave Background Data Analysis (LAMBDA). Support for LAMBDA is provided by the NASA Office of Space Science. The likelihood codes will be made public through LAMBDA (<http://lambda.gsfc.nasa.gov/>) and the ACT website (<http://www.physics.princeton.edu/act/>).

APPENDIX

In this Appendix, we perform additional tests on the CMB-only likelihood. In Fig 11 we show a selection of the distributions of the CMB bandpowers from the estimated $600 < \ell < 4500$ range. Distributions for the ACT-E and ACT-S bandpowers are compared to Gaussian distributions (dashed curves); bandpowers at $\ell > 3900$ are significantly non-Gaussian, but are well fit by Gaussians at larger scales. The same behaviour is found for the ACT-S bandpowers.

We then compare the secondary parameters estimated in two ways: (1) estimating CMB bandpowers, and (2) estimating 6 Λ CDM parameters. The distributions are shown in Fig 12, and are consistent. The tSZ, point source parameters, and Galactic cirrus parameters are not strongly affected by the CMB model assumptions. The kSZ power, a_{kSZ} , is $\sim 1\sigma$ lower in the model-independent case, as it is anti-correlated with the CMB bandpowers at $\ell > 2000$ due to the common blackbody dependence. The data cannot distinguish between lensed CMB power and kSZ power at $\ell \sim 3000$ scales, so the preference for a smaller kSZ value in the model-independent case is driven by the prior that the CMB power is positive. We test this by allowing the CMB bandpowers to take unphysical negative values. Here, the kSZ power increases to $a_{\text{kSZ}} < 12$ at 95% confidence, more consistent with the limits when Λ CDM is assumed.

REFERENCES

- Addison, G. E., Dunkley, J., & Bond, J. R. 2012a, ArXiv e-prints, 1210.6697
 Addison, G. E. et al. 2012b, ApJ, 752, 120, 1108.4614
 Addison, G. E., Dunkley, J., & Spergel, D. N. 2012c, MNRAS, 427, 1741, 1204.5927
 Battaglia, N., Bond, J. R., Pfrommer, C., & Sievers, J. L. 2012a, ApJ, 758, 75, 1109.3711
 Battaglia, N., Bond, J. R., Pfrommer, C., Sievers, J. L., & Sijacki, D. 2010, ApJ, 725, 91, 1003.4256
 Battaglia, N., Natarajan, A., Trac, H., Cen, R., & Loeb, A. 2012b, ArXiv e-prints, 1211.2832
 Bode, P., Ostriker, J. P., Cen, R., & Trac, H. 2012, ArXiv e-prints, 1204.1762
 Bond, J. R., Contaldi, C., Lewis, A., & Pogosyan, D. 2004, International Journal of Theoretical Physics, 43, 599, arXiv:astro-ph/0406195
 Bond, J. R., Contaldi, C. R., & Pogosyan, D. 2003, Phil. Trans. Roy. Soc. Lond., A361, 2435, astro-ph/0310735
 Bond, J. R., Jaffe, A. H., & Knox, L. 2000, ApJ, 533, 19, astro-ph/9808264
 Bridle, S. L., Crittenden, R., Melchiorri, A., Hobson, M. P., Kneissl, R., & Lasenby, A. N. 2002, MNRAS, 335, 1193
 Connolly, A. J. et al. 2002, ApJ, 579, 42, arXiv:astro-ph/0107417
 Das, S. et al. 2011, ApJ, 729, 62, 1009.0847
 Das, S., et al. 2013, submitted
 Dunkley, J., Bucher, M., Ferreira, P. G., Moodley, K., & Skordis, C. 2005, MNRAS, 356, 925, arXiv:astro-ph/0405462
 Dunkley, J. et al. 2011, ApJ, 739, 52, 1009.0866
 ——. 2009, ApJS, 180, 306, 0803.0586
 Dünner, R. et al. 2012, ArXiv e-prints, 1208.0050
 Efstathiou, G., & Migliaccio, M. 2012, MNRAS, 3051, 1106.3208
 Eriksen, H. K., Hansen, F. K., Banday, A. J., Górski, K. M., & Lilje, P. B. 2004, ApJ, 605, 14
 Finkbeiner, D. P., Davis, M., & Schlegel, D. J. 1999, ApJ, 524, 867, astro-ph/9905128
 Fowler, J. W. et al. 2010, ApJ, 722, 1148, 1001.2934
 Giallisco, M., Steidel, C. C., Adelberger, K. L., Dickinson, M. E., Pettini, M., & Kellogg, M. 1998, ApJ, 503, 543, arXiv:astro-ph/9802318
 Gispert, R., Lagache, G., & Puget, J. L. 2000, A&A, 360, 1, arXiv:astro-ph/0005554

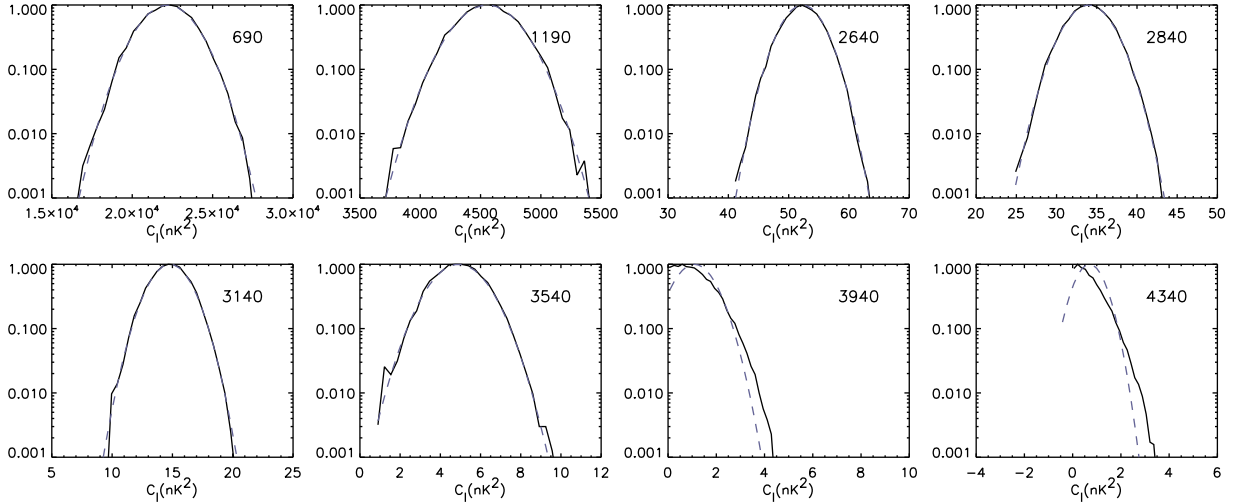


FIG. 11.— Probability distributions of a selection of CMB bandpowers for ACT-E in the range $600 < \ell < 4500$, marginalized over secondary parameters (solid). The bin-center for each bandpower shown is indicated on each panel. The bandpowers are well-approximated by Gaussian distributions (dashed), except at scales $\ell \gtrsim 3700$. The same behavior is seen for the ACT-S bandpowers.

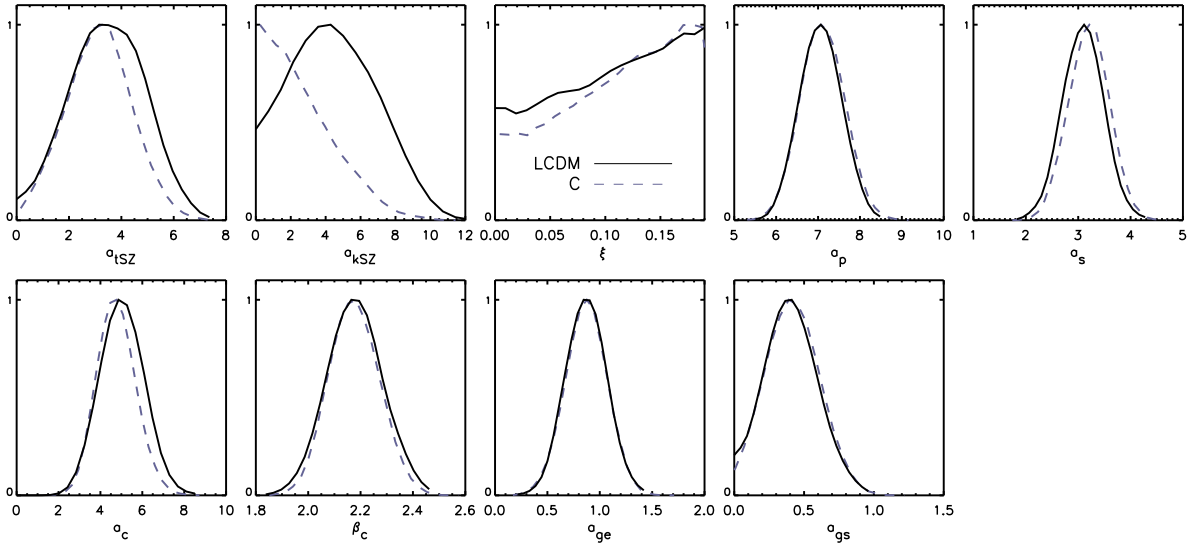


FIG. 12.— Secondary SZ and foreground parameters estimated assuming the Λ CDM model ('LCDM'), compared to the same parameters estimated jointly with primary CMB bandpowers ('C'). They are consistent, but an anti-correlation between the primary CMB bandpowers and the kSZ power leads to a reduction in a_{kSZ} in the latter case.

Gold, B. et al. 2011, ApJS, 192, 15, 1001.4555

Gralla, M., et al. 2013, in preparation

Gruzinov, A., & Hu, W. 1998, ApJ, 508, 435,

arXiv:astro-ph/9803188

Hajian, A. et al. 2011, ApJ, 740, 86, 1009.0777

—. 2012, ApJ, 744, 40, 1101.1517

Hall, N. R. et al. 2010, ApJ, 718, 632, 0912.4315

Hauser, M. G. et al. 1998, ApJ, 508, 25, arXiv:astro-ph/9806167

Hinshaw, G. et al. 2003, ApJS, 148, 135

Iliev, I. T., Mellema, G., Shapiro, P. R., & Pen, U.-L. 2007,

MNRAS, 376, 534, arXiv:astro-ph/0607517

Itoh, N., Kohyama, Y., & Nozawa, S. 1998, ApJ, 502, 7,

arXiv:astro-ph/9712289

Jewell, J., Levin, S., & Anderson, C. H. 2004, ApJ, 609, 1,

arXiv:astro-ph/0209560

Keisler, R. et al. 2011, ApJ, 743, 28, 1105.3182

Komatsu, E., & Seljak, U. 2002, MNRAS, 336, 1256

Komatsu, E. et al. 2011, ApJS, 192, 18, 1001.4538

Lagache, G., Bavouzet, N., Fernandez-Conde, N., Ponthieu, N.,

Rodet, T., Dole, H., Miville-Deschênes, M.-A., & Puget, J.-L.

2007, ApJ, 665, L89, 0707.2443

Larson, D. et al. 2011, ApJS, 192, 16, 1001.4635

Lewis, A., & Bridle, S. 2002, Phys. Rev. D, 66, 103511

Lewis, A., Challinor, A., & Lasenby, A. 2000, ApJ, 538, 473

Lueker, M. et al. 2010, ApJ, 719, 1045, 0912.4317

Marriage, T. A. et al. 2011, ApJ, 731, 100, 1007.5256

McQuinn, M., Furlanetto, S. R., Hernquist, L., Zahn, O., &

Zaldarriaga, M. 2005, ApJ, 630, 643, arXiv:astro-ph/0504189

Mesinger, A., McQuinn, M., & Spergel, D. N. 2012, MNRAS, 422,

1403, 1112.1820

Miville-Deschênes, M.-A., & Lagache, G. 2005, ApJS, 157, 302,

arXiv:astro-ph/0412216

Nolta, M. R. et al. 2009, ApJS, 180, 296, 0803.0593

Ostriker, J. P., & Vishniac, E. T. 1986, ApJ, 306, L51

Planck Collaboration I et al. 2011, A&A, 536, A1, 1101.2022

Planck Collaboration XIX et al. 2011, A&A, 536, A19, 1101.2029

Planck Collaboration XVIII et al. 2011, A&A, 536, A18,

1101.2028

- Puget, J.-L., Abergel, A., Bernard, J.-P., Boulanger, F., Burton, W. B., Desert, F.-X., & Hartmann, D. 1996, *A&A*, 308, L5
- Reichardt, C. L. et al. 2012, *ApJ*, 755, 70, 1111.0932
- Sehgal, N. et al. 2010, *ApJ*, 709, 920, arXiv:0908.0540
- Sharp, M. K. et al. 2010, *ApJ*, 713, 82, 0901.4342
- Shaw, L. D., Nagai, D., Bhattacharya, S., & Lau, E. T. 2010, *ApJ*, 725, 1452, 1006.1945
- Shaw, L. D., Rudd, D. H., & Nagai, D. 2012, *ApJ*, 756, 15, 1109.0553
- Shaw, L. D., Zahn, O., Holder, G. P., & Doré, O. 2009, *ApJ*, 702, 368, 0903.5322
- Shirokoff, E. et al. 2011, *ApJ*, 736, 61, 1012.4788
- Sievers, J., et al. 2013, submitted
- Sievers, J. L. et al. 2003, *ApJ*, 591, 599
- . 2009, ArXiv e-prints, 0901.4540
- Silk, J. 1968, *ApJ*, 151, 459
- Spiegel, D. N. et al. 2003, *ApJS*, 148, 175
- Story, K. T. et al. 2012, ArXiv e-prints, 1210.7231
- Sunyaev, R. A., & Zel'dovich, Y. B. 1970, 7, 3
- Swetz, D. S. et al. 2011, *ApJS*, 194, 41, 1007.0290
- Trac, H., Bode, P., & Ostriker, J. P. 2011, *ApJ*, 727, 94, 1006.2828
- Vieira, J. D. et al. 2010, *ApJ*, 719, 763, 0912.2338
- Viero, M. P. et al. 2009, *ApJ*, 707, 1766, 0904.1200
- Wandelt, B. D., Larson, D. L., & Lakshminarayanan, A. 2004, *Phys. Rev. D*, 70, 083511, arXiv:astro-ph/0310080
- Zahn, O. et al. 2012, *ApJ*, 756, 65, 1111.6386